Original Article

Author for correspondence:
Koushik Sen, Email: koushik.geol@gmail.com

CAMBRIDGE
UNIVERSITY PRESS

Understanding pre- and syn-orogenic tectonic evolution in western Himalaya through age and petrogenesis of Palaeozoic and Cenozoic granites from upper structural levels of Bhagirathi Valley, NW India

Aranya Sen[1], Koushik Sen[1,2] , Amitava Chatterjee[1,3] , Shubham Choudhary[1] and Alosree Dey[1,2]

[1]Wadia Institute of Himalayan Geology, 33 GMS Road, Dehradun-248001, India; [2]Academy of Scientific and Innovative Research, Ghaziabad-201002, India and [3]Faculty of Science, Banaras Hindu University, Varanasi, India

Abstract

The Himalaya is characterized by the presence of both pre-Himalayan Palaeozoic and syn-Himalayan Cenozoic granitic bodies, which can help unravel the pre- to syn-collisional geodynamics of this orogen. In the Bhagirathi Valley of Western Himalaya, such granites and the Tethyan Himalayan Sequence (THS) hosting them are bound to the south by the top-to-the-N extensional Jhala Normal Fault (JNF) and low-grade metapelite of the THS to its north. The THS is intruded by a set of leucocratic dykes concordant to the JNF. Zircon U–Pb laser ablation multi-collector inductively coupled plasma mass spectrometry (LA-MC-ICP-MS) geochronology of the THS and one leucocratic dyke reveals that the two rocks have a strikingly similar age distribution, with a common and most prominent age peak at ~1000 Ma. To the north of the THS lies Bhaironghati Granite, a Palaeozoic two-mica granite, which shows a crystallization age of 512.28 ± 1.58 Ma. Our geochemical analysis indicates that it is a product of pre-Himalayan Palaeozoic magmatism owing to extensional tectonics in a back-arc or rift setting following the assembly of Gondwana (500–530 Ma). The Cenozoic Gangotri Leucogranite lies to the north of Bhaironghati Granite, and U–Pb dating of zircon from this leucogranite gives a crystallization age of 21.73 ± 0.11 Ma. Our geochemical studies suggest that the Gangotri Leucogranite is a product of muscovite-dehydration melting of the lower crust owing to flexural bending in relation to steepening of the subducted Indian plate. The leucocratic dykes are highly refracted parts of the Gangotri Leucogranite that migrated and emplaced along extensional fault zones related to the JNF and scavenged zircon from the host THS during crystallization.

1. Introduction

The Himalaya is a result of continental collision between India and Eurasia and is characterized by both pre- and syn-Himalayan magmatism. The syn-Himalayan Cenozoic leucogranite can be divided into two types (King *et al.* 2011; Guo & Wilson, 2012). The Greater Himalayan Leucogranite (GHL) is present within and along the northern margin of the Himalayan metamorphic core or the Greater Himalayan Sequence (GHS), having ages ranging from ~25 to ~9 Ma. North of this GHL, along the North Himalayan Antiform, lies the chain of Tethyan Himalayan Leucogranites (THL), having an age range of ~23 to ~12 Ma. Both these chains of leucogranite are orogen-parallel and strike roughly east–west, with younger ages in the eastern parts of the Himalaya (Fig. 1a).

Both the source and petrogenesis of these suites of leucogranites have been a matter of conjecture. Some researchers opine that both Greater Himalayan and Lesser Himalayan components were involved in the generation of these leucogranites (Garzanti *et al.* 1986; Le Fort *et al.* 1987; Visonà & Lombardo, 2002). However, many others have suggested that the GHS was the sole contributor (Harris & Massey, 1994; Guillot & Le Fort, 1995; Harrison *et al.* 1999; Zhang *et al.* 2004). Guo & Wilson (2012) suggested that these leucogranites are derived from the bulk of the GHS crust with some amount of Lesser Himalayan fluid, while Hopkinson *et al.* (2017) argued that GHL is entirely formed by partial melting of the GHS.

Plausible petrogenetic models to explain the genesis of these leucogranites also vary from muscovite-dehydration melting (Patiño Douce & Harris, 1998; Phukon *et al.* 2019) to biotite-dehydration melting (Visonà & Lombardo, 2002; Visonà *et al.* 2012; Groppo *et al.* 2013) to decompression melting (Zhang *et al.* 2004, 2005) and water flux melting (Harris & Massey, 1994; Davidson *et al.* 1997). Thus, inferring a uniform source and postulating one single
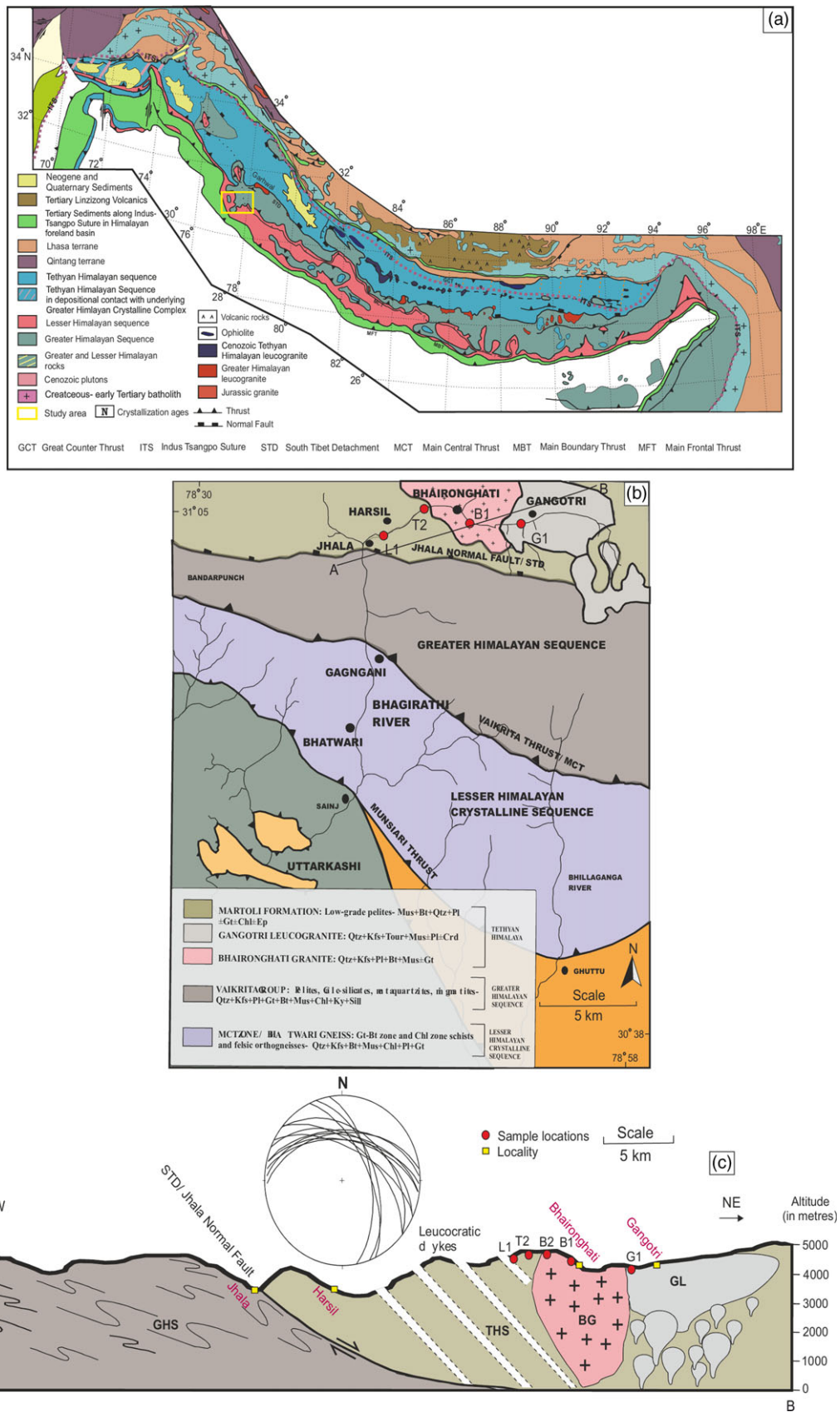
Fig. 1. (Colour online) (a) Generalized geological map of the Himalaya (modified after Yin, 2006). Yellow box represents the study area. (b) Geological map of the Bhagirathi Valley of Western Garhwal Himalaya, Uttarakhand (modified after Metcalfe, 1993). (c) Geological cross-section (AB) of the study area shown in (b). Locations and samples used for various analyses are also shown.

Table 1. Locations and types of samples used for analysis

Sample no.	GPS	Rock type and litho-units	Analysis*
T2	31° 05′ 44″″ N, 78° 53′ 25″ E	Low-grade garnetiferous mica schist (THS)	Petrography, geochemistry, U–Pb geochronology
L1	31° 05′ 39″ N, 78° 53′ 23″ E	Leucocratic dyke	Petrography, geochemistry, U–Pb geochronology
B1	31° 04′ 43″ N, 78° 54′ 16″ E	Two-mica granite (BG)	Petrography, geochemistry, U–Pb geochronology
B2	31° 04′ 39″ N, 78° 54′ 13″ E	Two-mica granite (BG)	Petrography
G1	31° 04′ 35″ N, 78° 54′ 49″ E	Tourmaline–muscovite granite (GL)	Petrography, geochemistry, U–Pb geochronology

*One common sample is used for U–Pb zircon geochronology and geochemistry. Three to four samples per lithology were used for petrography.

petrogenetic model for the Himalayan leucogranites can be misleading. These leucogranites need to be characterized in terms of their emplacement mode, relationship with host rocks, petrology and age along with tectonic setting to understand their evolution with respect to the Himalayan tectonics.

As well as the syn-collisional leucogranites, a separate batch of pre-collisional Palaeozoic two-mica granites is also present along-strike Himalaya, adjacent to the South Tibetan Detachment (STD). The source, emplacement mechanisms and the tectonic settings in which these plutons evolved are still a matter of debate. The origin of these granites is attributed to the final assembly of Gondwana (Meert & Van der Voo, 1997; Miller *et al.* 2001; Lee *et al.* 2006; Wang *et al.* 2012). Miller *et al.* (2001) suggested that they generated in a non-arc extensional domain, whereas Cawood *et al.* (2007) argued that these melts originated due to volcanic arc magmatism in a collisional setting. Robust geochemical analysis of widespread volcanic rocks (basalts, andesites and felsic rocks) along the margin of Gondwana in the Tethyan Himalaya (Valdiya, 1995), as well as within the Lhasa terrane, along the northern margin of Gondwana (Zhu *et al.* 2012), indicated volcanic-arc or arc-related magmatism as a cause for emplacement of these Palaeozoic granites. Combining geochemical and geochronological analysis, Wang *et al.* (2012) suggested that the entire span of this ~500 Ma magmatism can be attributed to volcanic arc and associated back-arc rift magmatism.

The Bhagirathi Valley of Garhwal Himalaya, India, is an ideal section from western Himalaya where both pre-collisional Palaeozoic two-mica granites and syn-collisional leucogranites and leucocratic dykes are present at various structural heights (Fig. 1b–c). For this study, we have carried out outcrop-scale and petrographic study coupled with geochemical (major, minor and trace element) and geochronological (zircon U–Pb laser ablation multi-collector inductively coupled plasma mass spectrometry (LA-MC-ICP-MS)) analyses of these aforementioned suites of two-mica granites, leucogranites and associated Tethyan rocks. Based on this information, we have postulated a comprehensive tectonic model to explain the geodynamics of this part of the Himalaya with respect to magmatism of different suites of granitic bodies.

2. Geology of the study area

In the Bhagirathi Valley, the Main Central Thrust (MCT), the major shortening accommodating the intra-terrane fault zone in the Himalaya, forms a ~12 km thick NNE-dipping shear zone that separates Lesser Himalayan Formations from the Vaikrita Group or the Greater Himalayan Sequence (Metcalfe, 1993; Fig. 1b–c). The GHS is a ~30 km package of metamorphic rocks composed of sillimanite- and kyanite-bearing garnetiferous schist/gneisses

(Metcalfe, 1993; Singh, 2003). At the structural top of the GHS, a N-dipping fault, the Jhala Normal Fault (JNF), forms the boundary between the GHS and the low-grade Tethyan Himalayan Sequence (THS). The grade of metamorphism increases towards the top of the GHS in a northward direction where sillimanite + K-feldspar gneisses are intercalated with foliated, anatectic granites (Metcalfe, 1993). Further north, overlying the GHS, is the lowest part of the THS, namely the Harsil Formation (R Pant, unpub. Ph.D. thesis, Roorkee Univ., 1986). The Harsil Formation / THS is low-grade metapelite. The JNF demarcates the southern margin of the study area. Different litho-units of the present study area are introduced in the following section.

The sample locations are plotted in Figure 1b. The sample locations, litho-unit/structural positions and various analytical techniques used for each sample are listed in Table 1. The collective dataset from the samples classifying the individual outcrops are THS (T2), leucocratic dyke (L1), Bhaironghati Granite (B1) and Gangotri Leucogranite (G1).

2. a. Jhala Normal Fault (JNF)

The Jhala Normal Fault (JNF) marks the boundary between the GHS and the THS. It has been a matter of conjecture whether the JNF is the actual South Tibetan Detachment, i.e. the regional tectonic boundary between the THS and GHS across the western and central Himalaya. The JNF activated after 15 Ma as constrained from the apatite fission track ages (Sorkhabi *et al.* 1999). Earlier mapping by Pêcher (1991) and a review by Yin (2006) suggested that Jhala is a N-directed brittle thrust zone superposed on a zone of dominantly N-verging ductile folds in garnet–biotite gneiss and schist. They also suggested that the actual STD is likely located at a higher structural level than the 'Jhala thrust' of Pêcher & Scaillet (1989) and the Jhala 'normal' fault of Metcalfe (1993). Metcalfe (1993) inferred that the JNF is a N-dipping normal fault separating the Greater Himalayan Crystallines (GHS) from the Tibetan–Tethyan sediments. He also suggested localized shear and the presence of normal-sense brittle offsets.

Metamorphic grade within the GHS increases towards the north until it reaches sillimanite/kyanite mica schist/gneiss before passing into migmatite (Scaillet *et al.* 1995; Singh, 2018). Our field observations suggest that further north, near Jhala (Fig. 1b), there is a complete change in lithology with the occurrence of very low-grade biotite/chlorite schist. A set of fractures trending NE and a set of local-scale N-verging folds appears within the THS. Fault gouges and cataclasites are well exposed in the road-cut section along the Jhala Bridge (Fig. 2a). Asymmetric quartz clast (Fig. 2b), mica-fish and quarter structures showing top-to-the-N shearing suggest deformation features related to extensional faulting.

Fig. 2. (Colour online) Outcrop-scale features. (a) Fault-gouges in the hanging wall of Jhala Normal Fault (JNF). (b) Quartz clasts within the THS showing top-to-the-N or down-dip shearing suggesting extensional movement. (c) Leucocratic dykes intruding the THS. (d) Asymmetric quartz boudins showing top-to-the-N / extensional shearing. (e) Close-up view of tourmaline-bearing leucocratic dyke intruding the THS. (f) Fault propagation fold near the contact of THS and BG. (g) Contact between BG and THS (marked as 'H'). (h) Typical coarse-grained two-mica granite of BG. (i) Mafic microgranitoid enclaves within the BG. (j) Contact between BG and GL. (k) GL intruding BG; biotite is completely absent, tourmaline occurs as blebs and clasts and some fractures are present randomly along which aplite veins appear.

2.b. Harsil Formation / THS and leucocratic dykes

The THS is intruded by a series of leucocratic dykes as we move structurally up-section (Fig. 2c). These dykes are 5–7 m thick and are at an inclination of 30–35° (see also Stern *et al.* 1989; Scaillet *et al.* 1995; Singh *et al.* 2003; Singh, 2018). Quartz clasts within the THS show top-to-the-N or down-dip shearing suggesting extensional faulting (Fig. 2d). These dykes are mainly composed of quartz–K-feldspar aggregates with muscovite and ample amounts of tourmaline (Fig. 2e). The orientation of these dykes is sub-parallel to the regional foliation. A large-scale en-echelon pattern is noted, as the majority of the garnet–tourmaline-bearing dykes are oriented NNW and dipping ENE. The dyke orientation may be a consequence of sliding at the top of the metamorphic pile (chlorite–biotite schist + leucogranite) toward the N or NW

during or after the leucocratic dyke injection (Scaillet *et al.* 1995, 1996). The low-grade metamorphic rocks of the THS are chlorite–biotite schists with a uniformly N-dipping penetrative foliation (R Pant, unpub. Ph.D. thesis, Roorkee Univ., 1986). These rocks have undergone very low-grade metamorphism, probably in the lower greenschist facies during activation of the JNF (Metcalfe, 1993), and are characterized by the presence of small-scale fault-propagation folds near the contact with the Bhaironghati Granite (Fig. 2f).

2.c. Bhaironghati Granite (BG)

The BG is present to the north of the THS. As noted by Stern *et al.* (1989), the petrographic and geochemical characteristics of this granite are very similar to those of the Cambro-Ordovician
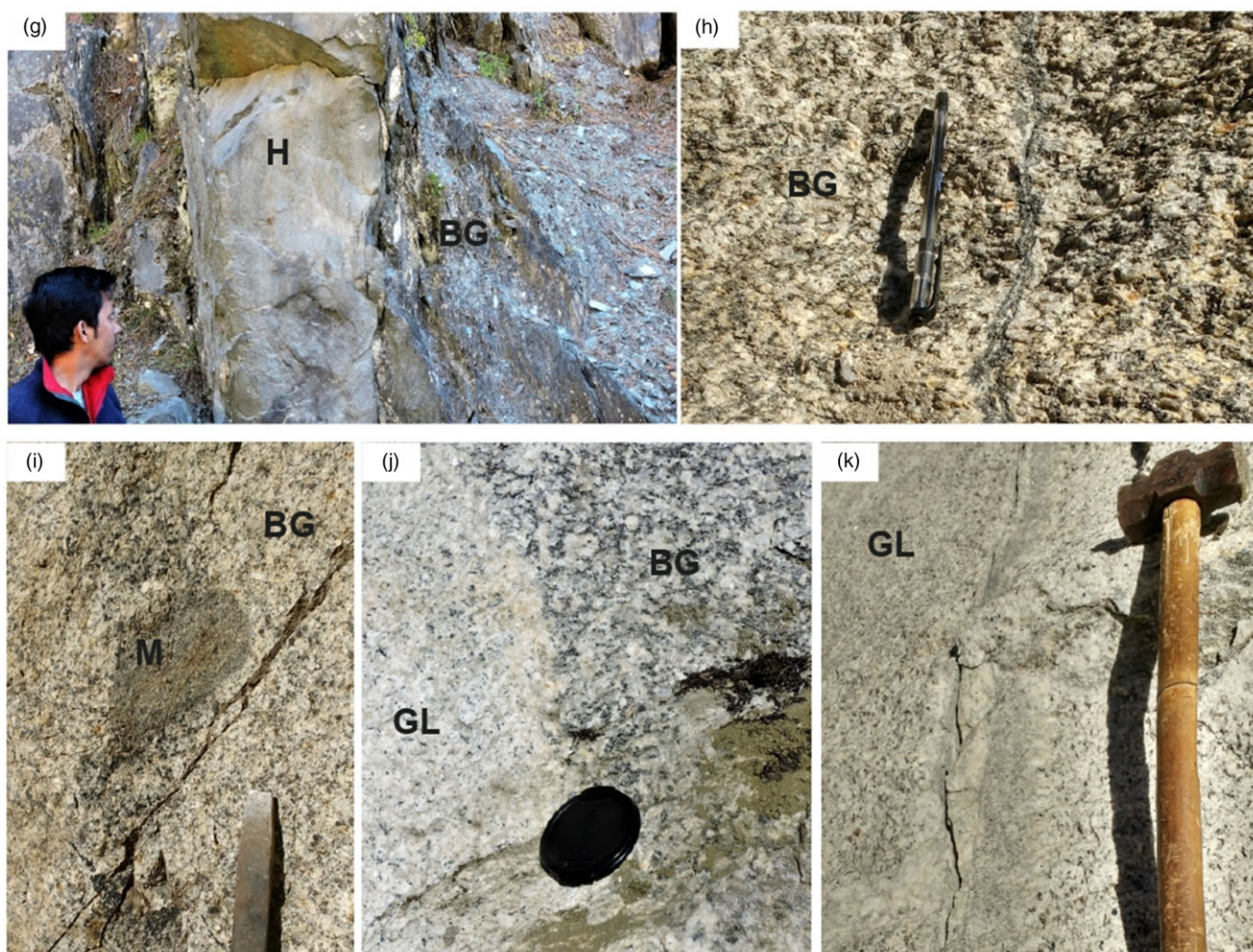
Fig. 2. (continued).

magmatism defined by Le Fort (1986) for the entire Himalayan belt. Stern *et al.* (1989) also reported that BG structurally underlies the tourmaline leucogranite and is spatially related to the upper part of the Tibetan Slab, whereas Scaillet *et al.* (1990) suggested that BG is located above the Tibetan slab. The BG first appears east of Harsil (Fig. 1b), having a sharp contact with the THS (Fig. 2g; Manickavasangam *et al.* 1999; Singh, 2003, 2018). It is a coarse-grained two-mica granite (Fig. 2h) and is characterized by mafic microgranitoid enclaves (Fig. 2i). We observed that, although the biotite–muscovite granite is deformed along its lower margins, the interior of the pluton is not at all deformed. Further north, this biotite–muscovite granite is cut by younger bodies of muscovite–tourmaline granite and garnet–beryl–tourmaline pegmatite (Fig. 2j), which are related to the overlying Gangotri Leucogranite.

2.d. Gangotri Leucogranite (GL)

Leucogranites from the upper Bhagirathi Valley make up several lenses or small plutons, 1.5–2 km thick and 4–5 km long, rather than a single body such as the Manaslu pluton (Scaillet *et al.* 1988). These lenses are intrusive either in the base of the THS or in the BG (R Pant, unpub. Ph.D. thesis, Roorkee Univ., 1986). The GL appears at the western end of the BG (Fig. 2j, k).

It is one of the largest Himalayan leucogranite plutons (Heim & Gansser, 1939; Gansser, 1964; Le Fort, 1975). It was first described by Heim & Gansser (1939) from the upper Alaknanda Valley, near Badrinath village. It was also recognized by Auden (1949) in the upper Bhagirathi Valley, who named it 'Gangotri granite'. In the present study area, it crops out as several lenses scattered over more than 400 km^2, each of which is several kilometres in length with laccolithic shape (Scaillet *et al.* 1990). Muscovite K–Ar ages of 18.4 ± 0.7 Ma were obtained from this leucogranite (Stern *et al.* 1989). The Th–Pb isotopic monazite age obtained is 22.4 ± 0.5 Ma (Harrison *et al.* 1997). Sorkhabi *et al.* (1999) carried out Ar–Ar dating on muscovite separates from the GL and obtained a plateau age of 17.9 ± 0.1 Ma.

The GL is usually characterized by a very weak foliation, defined by mica and tourmaline. The granite body is mainly massive with the presence of small-scale extensional fractures and aplite dykes near its contact with the BG. Near the contact, the foliation grades into layering which includes a few cm-thick bands of tourmaline (Singh, 2003). Tourmaline and muscovite are the dominant minerals apart from the quartzo-feldspathic aggregate. Muscovite is mainly enclosed within plagioclase and K-feldspar and its abundance generally decreases as we move away from the contact between GL and BG.

3. Petrography

3.a. T2

The THS (T2) is composed of sedimentary rocks that grade into low-grade metasediments in the vicinity of the JNF. Near the contact between the THS and BG, the appearance of subhedral garnet (Fig. 3a) suggests that a localized higher-order metamorphic event had taken place by accompanying the ductile deformation during the intrusion of the BG. This is also evident from the warping of biotite grains around garnet (Fig. 3a). Apart from this, the general mineral assemblage is quartz, K-feldspar, chlorite, biotite and rarely muscovite (Fig. 3b). Zircon, apatite and rutile occur as minor phases. Biotite and chlorite flakes occur in a preferred direction depicting the main transposed foliation.

3.b. L1

The leucocratic dyke (L1) has an assemblage of garnet + quartz + plagioclase + tourmaline ± muscovite ± sillimanite (Fig. 3c, d). Plagioclase grains have developed a fracture plane other than the prominent cleavage plane. Tourmaline is generally inclusion-free and is comparatively small in size. The muscovite flakes are comparatively large in size and oriented in a preferred direction. The presence of small homogeneous garnets (Fig. 3d) suggests their igneous origin. The appearance of sillimanite needles (Fig. 3c) suggests that the temperature during *in situ* melt intrusion was sufficiently high.

3.c. B1

BG (B1) is a coarse-grained rock exhibiting granular texture. It is mainly composed of quartz, plagioclase, K-feldspar, biotite and muscovite (Fig. 3e, f). This is basically a two-mica granite having well-defined boundaries of quartz. Plagioclase shows a concentric inclusion pattern and compositional zoning (Fig. 3f). Plagioclase, K-feldspar and mica occur mainly in euhedral to subhedral form. Garnet is present only along the contact of BG with the THS. One sample (B2) taken from the periphery of BG shows syn-kinematic garnet with mica warping around the garnet porphyroblast (Fig. 3e).

3.d. G1

GL is typically a tourmaline–muscovite leucogranite with quartz, K-feldspar and plagioclase occurring as the major phases and apatite and beryl as minor phases (Fig. 3g, h). Tourmaline grains contain numerous inclusions of quartz and plagioclase as well as apatite, but are totally free of K-feldspar inclusions. Muscovite is quite abundant (10–13 % modal) in this rock. It is mainly enclosed within quartz and K-feldspar and is always in textural equilibrium with other phases. However, rare overgrowth of muscovite on K-feldspar is present as typical symplectite texture. Biotite grains are rare and mostly enclosed within muscovite with a diffused boundary.

4. Analytical techniques

4.a. Bulk rock geochemistry

Major oxides and trace element concentrations were measured, using pressed powder pellets made with 7 g rock powder, by WDXRF (Bruker S8 Tiger) at the Wadia Institute of Himalayan Geology. Representative samples were crushed and pulverized up to 200 mesh size using an agate carbide ring grinding bowl.

Polyvinyl alcohol was mixed as a binding agent with the rock powder to make the pressed pellets. A separate 0.5 g powder of each sample was heated at 1000 °C for 8 hours to determine the loss-on-ignition (LOI). Analytical accuracies for major elements and trace elements are well within ±2–3 % and ±5–6 % respectively. International reference samples GA, GH, GSN, MA-N (CRPG, France), G-2, GSP-1, RGM-1, AGV-1 (USGS, USA) and JG-2, JG1-a and JA-2 (GSJ, Japan) were used to check precision and accuracy. A modified Lucas-Tooth & Pyne (1964) model with intensity-based matrix correction was used to derive the calibration coefficients.

An ICP-MS (Perkin-Elmer SCIEX ELAN DRC-e) was used at the Wadia Institute of Himalayan Geology to determine the rare-earth element (REE) concentrations for these same samples. An open-system digestion method was used to prepare the sample solution for REE analysis. Individual samples were powdered, 0.1 g from each sample was separately mixed in HF and HNO_3 (2:1 ratio) solution in Teflon crucibles and they were heated over a hot plate until the powdered samples were completely digested. Accuracy ranges between 2 and 12 %, and precision varies between 1 and 8 % in case of REE analysis. JG-2 and MB-H are the rock standards used to calibrate the ICP-MS instrument.

4.b. Zircon U–Pb LA-MC-ICP-MS dating

Zircon U–Pb LA-MC-ICP-MS dating was carried out for one Gangotri Leucogranite (G1), one Bhaironghati Granite (B1), one low-grade metasedimentary rock of the THS (T2) and one leucocratic dyke sample (L1). A total of ~3–4 kg of rock samples was crushed and processed using a jaw crusher, disc mill, Holman Wilfley water table, isodynamic magnetic separator and heavy liquids to separate the zircon required. Thereafter, zircon was hand-picked under stereo microscope and was mounted in PFA® Teflon. Mounted zircon was polished using 8, 5, 3, 1 and 0.25 micron diamond paste. Cathodoluminescence (CL) images of mounted zircon were obtained using a Gatan Chroma CL UV attached to a Zeiss EVO 40 EP scanning electron microscope with a varying probe current of 10–20 nA at the Wadia Institute of Himalayan Geology. The U–Pb geochronology for the selected four samples was carried out at the LA-MC ICP-MS facility, Wadia Institute of Himalayan Geology. It consists of MC-ICPMS (Neptune-plus, ThermoFisher Scientific Inc.) and a 193 mm excimer laser (UV Laser, Model Analyte G2, Cetec-Photon machine Inc.), equipped with a high-performance HelEx-II sample chamber. The methodology adopted is similar to that of Phukon *et al.* (2019). The analyses were carried out with energy density 4 J cm^{-2}, a repetition rate of 5 Hz, 75 % laser intensity and 175 total shots per analysis, i.e. 35 s analysis time for each spot with 10 s background measurement.

On the basis of the zoning pattern as revealed by the CL images of every sample, the spots were chosen. The spot sizes were fixed at 20 microns on the chosen zircon for U–Pb analysis. Zircon U–Pb downhole fractionation was corrected by using Z91500 as primary zircon standard. The normalization data for this primary standard is 1062.32 ± 2.22 Ma ($^{206}Pb/^{238}U$ age) [2 sigma, thermal ionization mass spectrometry (ID-TIMS)] (Wiedenbeck *et al.* 1995). For the sake of accuracy, Plešovice zircon grains having a concordant age of 337.13 ± 0.37 Ma (ID-TIMS; Sláma *et al.* 2008) were used. In our analyses, Z91500 and Plešovice provide the average normalized $^{206}Pb/^{238}U$ ages of 1063.4 ± 1.7 Ma (0.16 %; MSWD = 0.85; 2σ; probability fit = 0.75; n = 44) and 340.6 ± 1.1 Ma (0.32 %; MSWD = 1.15; 2σ; probability fit = 0.23; n = 40) respectively.
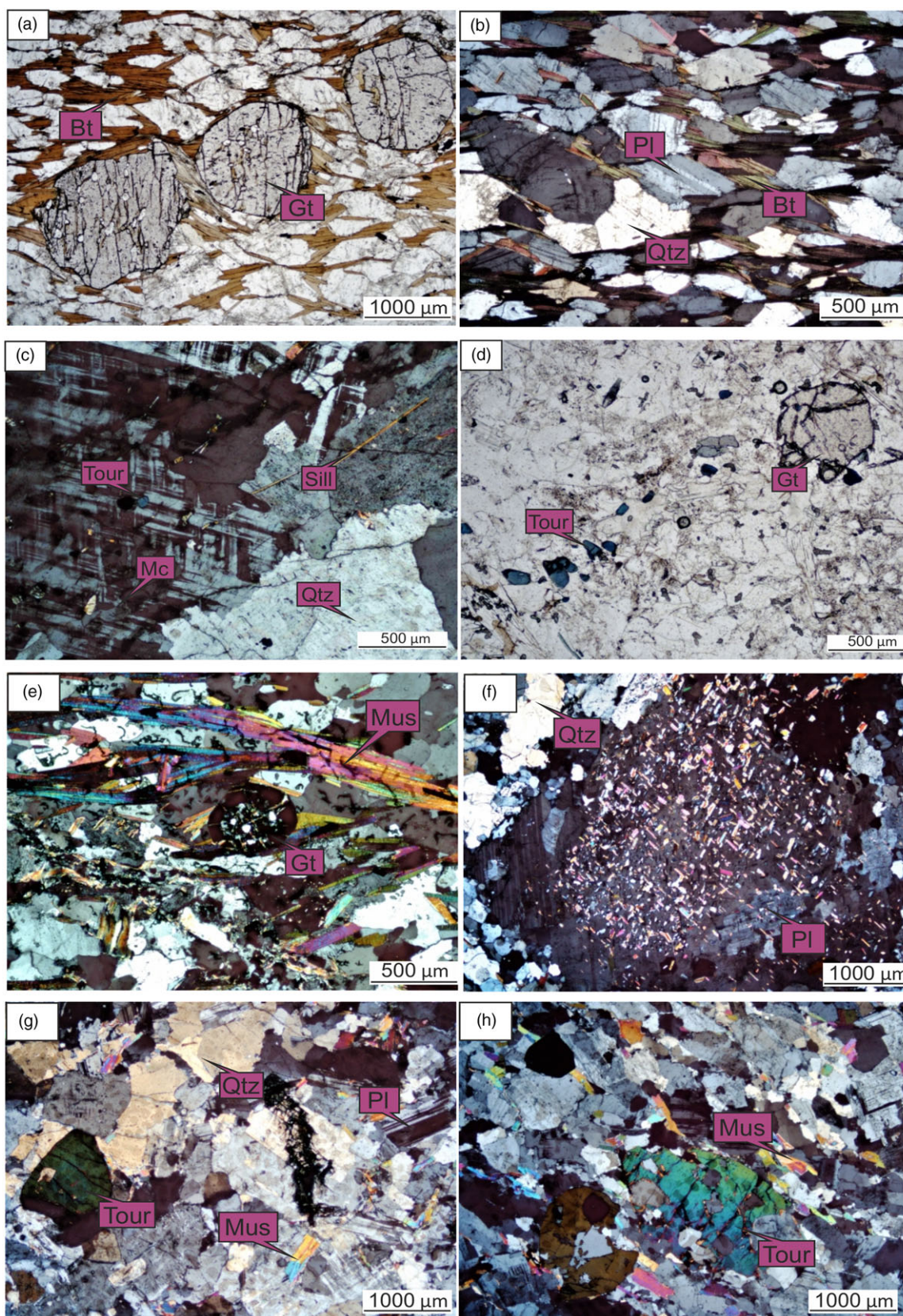
Fig. 3. (Colour online) Photomicrographs of representative samples (T2, L1, B1, G1). (a) Sample from the THS near its contact with the BG (T2-B) showing garnet–biotite assemblage along with a quartzo-fedspathic mass. (b) THS away from contact (T2-A) with BG showing mineral assemblage of quartz, K-feldspar, plagioclase and biotite. (c, d) Leucocratic dykes showing presence of garnet, plagioclase, quartz, tourmaline and sillimanite. (e) BG near its contact with the THS (BG-2) showing presence of garnet porphyroblast warped by a tectonic foliation defined by muscovite. (f) Plagioclase from interior part of BG (BG-1) showing concentric inclusion pattern and compositional zoning. (g, h) Sample from GL showing presence of plagioclase, quartz, muscovite and tourmaline. The mineral abbreviation scheme adopted is as follows: Gt (Garnet), Bt (Biotite), Mus (Muscovite), Pl (Plagioclase), Mc (Microcline), Tour (Tourmaline), Sill (Sillimanite) and Qtz (Quartz).

At the beginning and end of the analytical session, four analyses of each zircon standard were carried out and after every 10 analyses of unknown zircon grains from the studied samples, another two analyses of zircon standards were performed. Data reduction and plotting of data were carried out using Iolite software (Paton *et al.* 2011) and online IsoplotR software (Vermeesch, 2018). Cup configuration and parameters for the LA and MC-ICPMS (Chang et al. 2006; Gehrels *et al.* 2008;) are provided in Supplementary Material 1 (available online at https://doi.org/10.1017/S0016756821000789). The data-point error ellipse as well as the age uncertainties are quoted as 2σ error (Horstwood *et al.* 2016; Spencer *et al.* 2016).

5. Results

5.a. Bulk rock geochemistry

The complete dataset representing major, trace and REE concentrations of respective samples from different lithologies is provided in Table 2. Major element contents indicate that the GL and BG are peraluminous with aluminium saturation index (ASI = molecular ratio of $Al_2O_3/(CaO + Na_2O + K_2O)$; Shand, 1943) of 1.01–1.15 and 1.1–1.32 respectively (Fig. 4a). GL has high SiO_2 (71.66–72.45 wt %) and Al_2O_3 (15.25–15.76 wt %) and low MgO (0.10–0.14 wt %) contents (Table 2). The Na_2O concentrations in GL (4.21–4.46 wt %) are similar to those of K_2O (5.25–5.30 wt %; Table 2). BG has relatively low Na_2O (2.52–3.42 wt %) and high CaO (0.9–2.22 wt %) as compared to GL. However, the leucocratic dyke is highly silicic and oversaturated. The Rb vs Ba vs Sr plot (after El Bouseily & El Sokkary, 1975) suggests that GL is a product of strong differentiation (Fig. 4b). Based on the classification of Frost *et al.* (2001), GL can be called ferroan and alkalic to calc-alkalic, and plots within the field for peraluminous leucogranites. This indicates that GL is a product of crustal melts. The $Al_2O_3 - (Na_2O + K_2O)$ vs CaO vs FeO + MgO plot suggests that both the BG and GL are S-type granites (Fig. 4c). In the Rb/Sr vs Ba diagram (Inger & Harris, 1993), GL follows a muscovite vapour-absent trend as compared to the leucocratic dykes which follows a muscovite vapour-present trend (Fig. 4d). Feldspar fractionation trends (Fig. 4e–f) show dominantly K-feldspar fractionation for BG and plagioclase fractionation trend for GL.

GL is characterized by light REE (LREE) enrichment and negative Eu anomalies in chondrite-normalized REE patterns (Fig. 5a). BG is characterized by higher chondrite-normalized REE abundances compared to GL, though with broadly similar patterns. Relative to BG, GL has lower ΣREE, LREE and HREE contents, and lower La/Yb and Gd/Yb ratios. The leucocratic dyke, which is hosted within the THS, is highly silicic (SiO_2 = 74.44–75.6 wt %) and sodic (Na_2O = 5.54–5.6 wt %). Compared to GL, these dykes have lower ΣREE, lower K_2O and equivalent Fe_2O_3 contents (Table 2). These dykes are also peraluminous. The leucocratic dyke is characterized by a higher Fe_2O_3, MgO, CaO and TiO_2 content (Table 2). It also has lower Sr, Ba, Zr contents and lower Sr/Y, Zr/Hf ratios, but higher Rb concentrations and Rb/Sr ratios with respect to the GL (Fig. 5a). It is moderately enriched in LREE elements and has strong negative Eu anomaly (Fig. 5a). The $(Rb - Y + Nb) - (Rb - Y)$ tectonic discrimination diagram suggests that BG is a product of WPG (Within Plate Granite) magmatism whereas GL is a product of syn-COLG (syn-collisional) magmatism (Fig. 5b). Compared with the two-mica BG, GL has higher Al_2O_3, Na_2O, P_2O_5 and Rb contents, and lower Fe_2O_3, MgO, CaO, K_2O, TiO_2, Ba, Sr, Th, Zr and Y contents at a given SiO_2 content (Fig. 6; Table 2).

One representative sample from the THS was also analysed. It is characterized by low SiO_2 content (59.84 wt %) and moderate Na_2O, K_2O, CaO and Al_2O_3 content, along with high concentration of Ba and trace elements and low Rb/Sr ratio.

5.b. Zircon U–Pb LA-MC-ICP-MS dating

Zircon U–Pb LA-MC-ICP-MS dating was carried out on one representative sample from each lithology. These lithologies include the THS (sample T2), leucocratic dyke (sample L1), BG (sample B1) and GL (sample G1). Based on the internal structures as revealed by the CL images (Fig. 7), the core and rim of the zircon grains were identified and targeted for U–Pb spot analysis. The analytical data of zircon U–Pb LA-MC-ICP-MS dating are presented in Table 3. We refrain from using any arbitrary discordance percentage to filter the dataset for the detrital and igneous zircon. Rather, we evaluate the uncertainty of each and every spot age in conjunction with the concordia to distinguish between the concordant and discordant ages. Even if the centroid of a spot age does not fall on the concordia line, its uncertainty may overlap with the concordia line. These overlapping spot ages along with the centroid that fell on the concordia line were considered as the valid ages for various statistical calculations and plotting, as discussed in Spencer *et al.* (2016).

5.b.1. THS (sample T2)

The zircon grains are euhedral to subhedral, and mostly prismatic and elongated in nature. They usually have a length of ~200–100 μm and an aspect ratio of 1.3–1.45 (Fig. 7a). The majority of the grains are oscillatory zoned where the cores have brighter CL response. Rarely, patchy zoning is also observed (Fig. 7a). Out of 45 points from 42 grains, 8 spots were found to be concordant, and the majority of them were clustered around ~1000 Ma (Fig. 8a, b). U and Th contents range between 73.3 and 1436 ppm and 36.9 and 587 ppm, respectively. Th/U ratios of zircon grains range from 0.068 to 1.267 (Fig. 8a). The kernel density estimations of these concordant points reveal the most pronounced peak at ~1000 Ma (Fig. 8b).

5.b.2. Leucocratic dyke (sample L1)

Further north, in the central part of the THS (Fig. 1b), the leucocratic dykes cross-cut the THS. One sample from a leucocratic dyke (sample L1, close to sample T2) was analysed. The zircon grains are relatively small (~70–90 μm), but elongated and euhedral to subhedral in nature (Fig. 7b). The grains exhibit mostly homogeneous CL response (Fig. 7b). Sector zoning is rare (Fig. 7b). In total, 29 spots were analysed from 21 grains. Out of these, 10 points were found to be concordant. U and Th contents range between 112.6 and 1044 ppm and 26.58 and 586 ppm, respectively. Th/U ratios of the zircon grains range between 0.106 and 1.19 (Fig. 8c). All the data points reveal a similar age distribution to sample T2 (Fig. 8c). The kernel density estimation also reveals similar age-peaks with the most dominant age peak at ~1000 Ma (Fig. 8d).

5.b.3. BG (sample B1)

Zircon grains are prismatic and elongated (aspect ratio ~1:1.4 to ~1:1.45) with length varying between ~70 and 250 μm (Fig. 7c). The zircon grains are euhedral to subhedral in nature (Fig. 7c). These grains are mostly homogeneous under CL response. However, some grains exhibit a weak oscillatory and patchy zoning pattern (Fig. 7c). U and Th contents range between 107.7 and 5250

Table 2. Major, trace and REE data for the samples of THS/THS (T2), leucocratic dyke (L1), Bhaironghati Granite (B1) and Gangotri Leucogranite (G1). Normalization values for trace element are after Taylor and McLennan (1985)

	ALG1	ALG2	GL7	GL6	GL4	GL11	B2	B3	B1	B7	B4	B5	PLS1	PLS2	PLS3	LS7	LS4	LS6
Sample			Gangotri Leucogranite						Bhaironghati Granite						Leucocratic dyke			
Na_2O	4.21	4.46	4.41	4.27	4.33	4.39	2.74	2.52	2.89	2.63	2.94	3.42	0.83	0.66	0.65	0.74	0.69	0.68
MgO	0.14	0.10	0.12	0.13	0.11	0.14	0.32	1.25	0.71	0.79	0.41	0.83	0.05	0.03	0.03	0.04	0.03	0.04
Al_2O_3	15.76	15.25	15.36	15.53	15.26	15.65	14.47	15.47	14.87	14.39	13.82	15.66	1.20	0.13	0.04	0.73	1.05	0.27
SiO_2	71.81	72.36	71.56	72.45	71.66	71.93	72.52	68.47	70.55	69.58	73.49	68.13	>95.90	>95.90	>95.90	>95.90	>95.90	>95.90
P_2O_5	0.34	0.27	0.29	0.31	0.28	0.3	0.07	0.15	0.11	0.12	0.05	0.11	BDL	BDL	BDL	BDL	BDL	BDL
K_2O	5.30	5.25	5.28	5.27	5.26	5.29	5.03	4.9	4.36	4.57	6.08	5.29	0.07	0.02	BDL	0.03	0.01	BDL
CaO	0.77	0.70	0.73	0.72	0.74	0.75	1.02	2.17	2.22	1.94	0.9	2.11	0.13	0.01	BDL	0.05	BDL	0.07
TiO_2	0.14	0.10	0.11	0.13	0.12	0.13	0.28	0.65	0.41	0.36	0.17	0.4	0.02	0.03	BDL	0.01	0.02	0.01
MnO	0.01	0.01	0.01	0.01	0.01	0.02	0.06	0.07	0.05	0.06	0.03	0.05	BDL	BDL	BDL	BDL	BDL	BDL
Fe_2O_3	0.79	0.53	0.57	0.65	0.68	0.71	2.87	4.62	3.44	3.67	1.41	3.05	BDL	BDL	BDL	BDL	BDL	BDL
SUM	99.27	99.03	98.44	99.47	98.45	99.31	99.38	98.27	99.61	99.23	99.3	99.05	2.30	0.88	0.72	1.6	1.8	1.07
LOI	1.03	0.87	0.82	0.83	0.77	0.79	0.82	0.8	0.54	0.63	0.61	0.67	0.29	0.21	0.19	0.23	0.17	0.24
Ba	246	264	256	248	268	259	216	830	793	674	476	809	23.255	11.656	13.928	15.346	17.763	16.597
Cr	8	10	9	8	10	9	18	22	20	21	14	15	19	28	27	23	21	25
V	5	3	3	4	5	4	20	74	46	43	13	42	44.004	41.531	40.633	42.475	43.563	42.657
Sc	4	3	3	4	3	4	4	8	6	5	4	6	3	1	1	2	1	2
Co	15	25	24	15	25	19	3	66	9	13	32	20	71	41	48	56	49	51
Ni	BDL	BDL	BDL	BDL	BDL	BDL	4	9	6	7	1	5	BDL	BDL	BDL	BDL	BDL	BDL
Cu	8	7	6	8	7	6	3	8	4	4	1	9	5	5	2	4	3	3
Zn	62	45	54	59	57	61	59	56	44	48	24	40	BDL	1	BDL	1	1	1
Ga	33	29	31	30	29	28	20	16	17	16	13	17	BDL	BDL	BDL	BDL	BDL	BDL
Pb	51	59	55	56	55	53	30	23	24	27	39	30	3	BDL	BDL	1	2	1
Th	9	11	12	11	10	11	41	19	20	26	33	22	0.855	0.384	0.68	0.571	0.476	0.678
Rb	374	372	375	373	375	372	345	191	182	236	221	203	18.979	9.052	15.251	13.762	12.985	14.734
U	22.9	22.7	23.2	23.3	22.8	23.1	BDL	3.5	3	2.5	5.5	5.6	0.485	0.173	0.504	0.429	0.438	0.369
Sr	56	60	58	59	57	58	47	115	111	124	98	109	8.958	9.678	5.653	7.941	8.546	7.637
Y	44	43	44	42	43	41	49	32	33	37	52	34	1.714	0.533	1.963	0.745	1.547	0.868
Zr	57	58	55	59	58	56	113	162	174	113	126	154	BDL	BDL	BDL	BDL	BDL	BDL
Nb	18	15	16	17	15	18	11	13	11	12	8	10	2.159	0.451	0.533	1.489	0.758	1.156
La	3.816	4.346	4.254	3.976	3.896	3.827	25.27	41.58	36.4	34.29	32.45	39.21	1.715	0.467	1.255	0.782	1.376	1.235
Ce	9.425	10.128	10.078	9.769	10.065	9.532	55.86	88.04	76.43	73.65	69.13	64.86	3.932	1.801	2.62	1.785	2.548	1.875

(*Continued*)

Table 2. (*Continued*)

Sample	Gangotri Leucogranite						Bhaironghati Granite						Leucocratic dyke					
	ALG1	ALG2	GL7	GL6	GL4	GL11	B2	B3	B1	B7	B4	B5	PLS1	PLS2	PLS3	LS7	LS4	LS6
Pr	1.143	1.179	1.157	1.153	1.152	1.164	6.77	10.61	9.04	7.74	10.56	8.45	0.417	0.108	0.318	0.279	0.286	0.254
Nd	4.197	4.207	4.209	4.196	4.201	4.203	24.68	39.06	32.68	29.57	34.75	35.47	1.67	0.408	1.104	0.587	1.298	1.126
Sm	1.257	1.192	1.224	1.215	1.203	1.197	5.83	7.75	6.67	6.25	7.48	5.96	0.391	0.079	0.386	0.163	0.288	0.231
Eu	0.245	0.219	0.221	0.232	0.229	0.235	0.54	1.39	1.08	1.14	1.04	0.79	0.084	0.067	0.053	0.062	0.072	0.069
Gd	1.531	1.214	1.378	1.433	1.394	1.427	5.71	8.14	6.99	6.54	7.38	7.46	0.296	0.073	0.233	0.176	0.275	0.187
Tb	0.315	0.233	0.269	0.304	0.303	0.285	0.85	1.16	0.98	0.89	1.31	1.07	0.046	0.011	0.038	0.026	0.034	0.032
Dy	1.92	1.437	1.561	1.574	1.738	1.672	4.04	6.5	5.46	4.74	5.26	5.57	0.258	0.072	0.259	0.187	0.195	0.159
Ho	0.371	0.299	0.334	0.323	0.297	0.348	0.67	1.31	1.09	0.96	1.13	1.25	0.06	0.017	0.066	0.039	0.043	0.048
Er	0.974	0.853	0.879	0.927	0.933	0.886	1.46	3.32	2.74	2.43	2.89	3.08	0.179	0.15	0.226	0.148	0.196	0.201
Tm	0.16	0.152	0.156	0.158	0.157	0.159	0.2	0.48	0.38	0.29	0.22	0.31	0.034	0.01	0.046	0.028	0.031	0.037
Yb	1.096	1.107	1.102	1.098	1.097	1.106	1.25	3.02	2.23	2.46	2.65	2.86	0.254	0.076	0.346	0.176	0.189	0.232
Lu	0.177	0.195	0.186	0.187	0.185	0.182	0.17	0.41	0.31	0.25	0.34	0.29	0.047	0.015	0.067	0.028	0.034	0.053

ppm and 74.4 and 3230 ppm, respectively, whereas Th/U ratios vary between 0.073 and 0.615 (Fig. 9a). A total of 38 spots were analysed from 29 grains. In the Wetherill concordia diagram, the majority of the data were clustered around ~500 Ma (Fig. 9a). Fourteen spots of ~500 Ma age were found to be concordant (Fig. 9b). A weighted mean average of 512.28 ± 1.58 Ma (MSWD = 0.22) age was obtained from nine of the concordant points, which was inferred as the crystallization age of the BG (Fig. 9b).

5.b.4. GL (sample G1)

Zircon grains of GL (sample G1) are generally prismatic and elongated (aspect ratio ~1:1.3 to ~1:1.4), with length varying between ~45 and 140 μm. In CL images, the zircon grains reveal a weak oscillatory zoning pattern, where a brighter core is mantled by a dark and homogeneous rim (Fig. 7d). Rarely, dark and chaotically zoned cores are also present. U and Th contents range between 200 and 32 400 ppm and 199.9 and 9200 ppm, respectively. U content of the zircon grains from this sample is higher than in the other samples. Th/U ratios of zircon from this sample range from 0.01 to 1 (Fig. 9c). A total of 29 spots were analysed from 25 grains. Out of these 29 spots, only 5 spots near ~20 Ma were found to be concordant. A Wetherill concordia diagram reveals that the majority of the data points are clustered at ~20 Ma (Fig. 9c). The weighted average of these five concordant points is calculated as 21.73 ± 0.11 Ma (MSWD = 2.68; Fig. 9d).

U and Th concentrations of GL and BG are comparatively higher than those of the THS or leucocratic dykes. Th and U are heat-producing elements within the Earth's crust and sequestration. The mobilization of these elements is controlled by their partitioning into respective accessory minerals (Bea, 2012; Yakymchuk & Brown, 2019). Th/U ratios plotted against $^{206}Pb/^{238}U$ suggest that the GL and BG have dominantly igneous zircon with Th/U ratio >0.1. On the other hand, both the THS and the leucocratic dyke contain both igneous and metamorphic zircon of variable ages (Fig. 9e).

6. Discussion

6.a. Tectonic significance of the Jhala Normal Fault and its relationship with the Tethyan Himalayan Sequence

Our field and petrographic evidences (Figs 2a, b, c, e, f, 3a, b) indicate that northward progression across the JNF leads to abrupt changes in rock lithology along with an exponential decrease in metamorphic gradations. Moreover, it can be argued that the JNF is a NNE-directed low-angle normal fault zone. Excluding the changes in lithology and metamorphic grade, outcrop-scale features such as quarter structures, small mica fishes, quartz fish with top-to-the-N sense of shear, and the presence of abundant fault gouges in the riverbank sections corroborate this notion. We infer that the JNF is either the actual STD or one of its major splays that demarcates the boundary between high-grade metamorphic rocks of the Greater Himalaya and the low-grade THS. Our inferences, thus, are more in accordance with those of Metcalfe (1993) than those envisaged by Pêcher & Scaillet (1989) and Pêcher (1991), which suggest that the JNF is a brittle thrust zone.

Ages derived from one sample of the THS (sample T2) reveal the presence of detrital zircon between ~1050 and 900 Ma, with a pronounced peak at ~1000 Ma (Fig. 8a, b). Some older Archaean/Palaeoproterozoic ages are also present that suggest the presence of
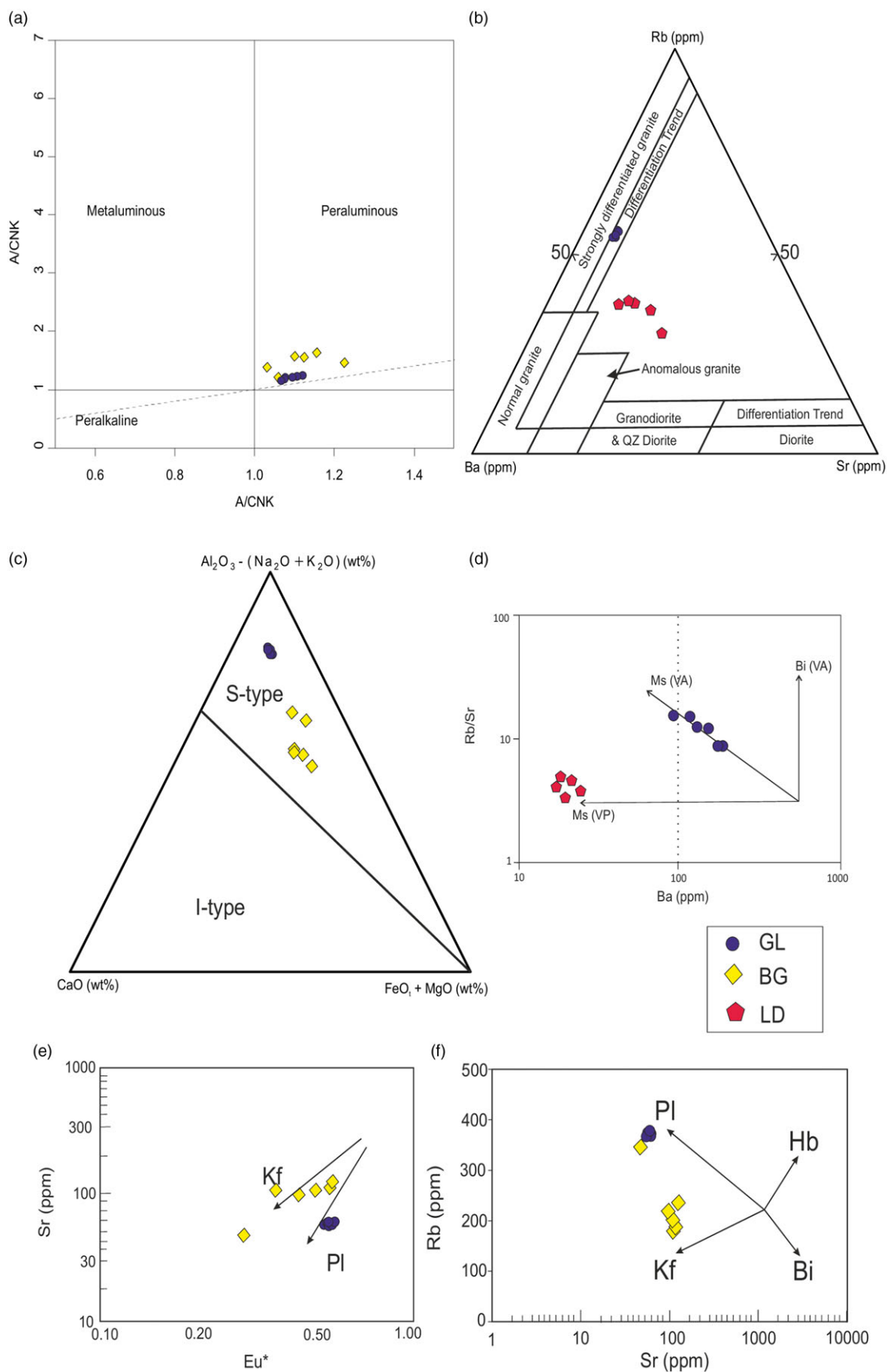
Fig. 4. (Colour online) (a) ACNK-ANK diagram for samples from GL and BG indicating the aluminium saturation index (ASI) (after Shand, 1943). (b) Classification under the Rb vs Ba vs Sr diagram to decipher the differentiation trends of GL and leucocratic dykes (after El Bouseily & El Sokkary, 1975). (c) $Al_2O_3 - (Na_2O + K_2O)$ vs CaO vs $FeO_t + MgO$ diagram for both BG and GL (after Inger & Harris, 1993). (d) Rb/Sr ratios vs Ba diagram. Ms (VP), Ms (VA) and Bt (VA) showing trends of vapour-present muscovite melting, vapour-absence muscovite and biotite melting, respectively (Inger & Harris, 1993) for GL and LD (leucocratic dyke). (E) Sr (ppm) vs Eu* diagram to decipher the fractionation of feldspar variety in BG and GL. (F) Rb vs Sr (ppm) to decipher the fractionation of feldspar in BG and GL.
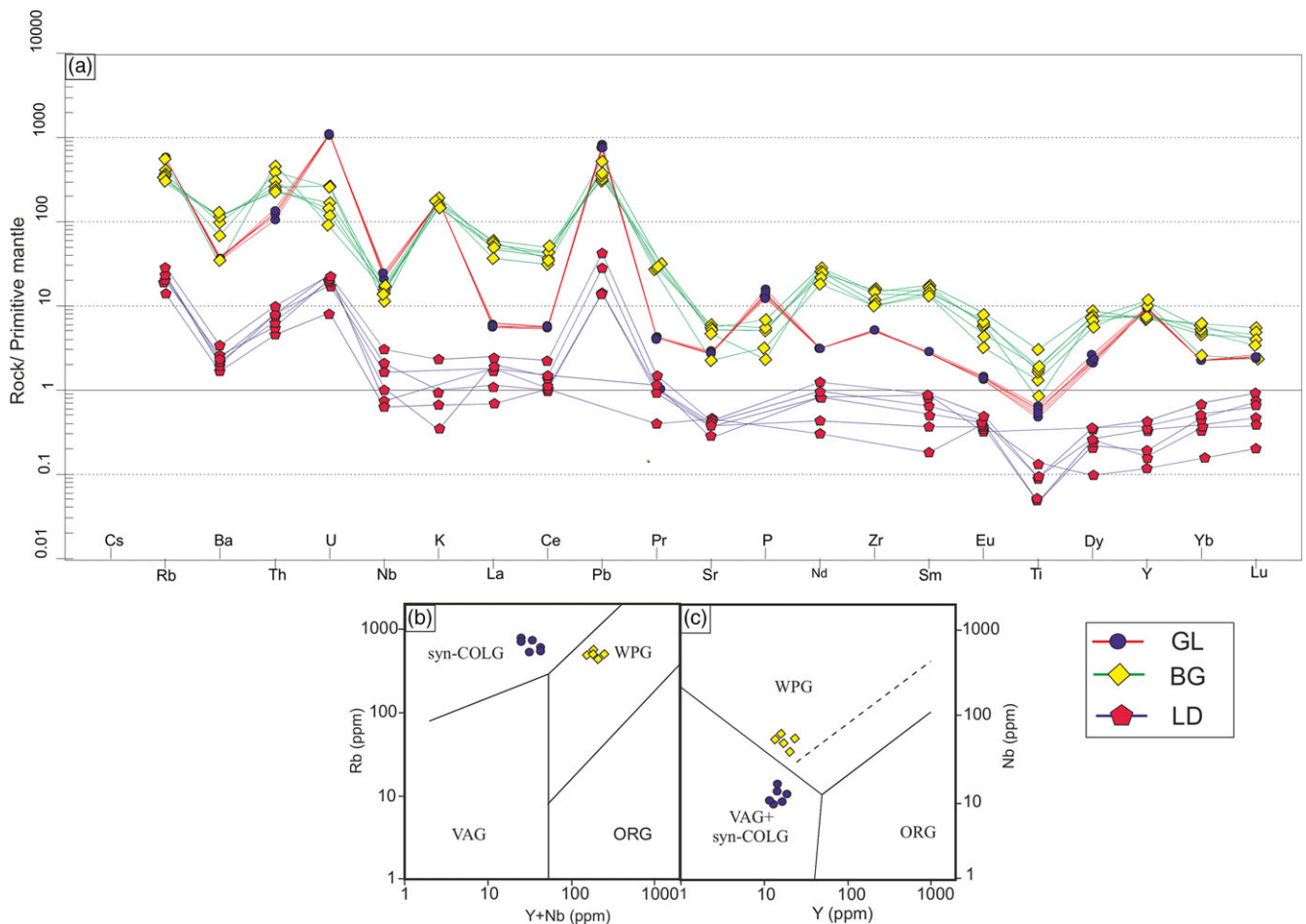
Fig. 5. (Colour online) (a) Primitive-mantle and chondrite-normalized REE plots (combined) for the same samples (after Boynton, 1984) depicting distinct anomaly patterns of REEs in BG and GL with respect to that of LD. (b) (Rb − Y + Nb) tectonic discrimination diagram differentiating BG and GL (after Pearce *et al.*, 1984). (c) (Rb − Y) tectonic discrimination diagram differentiating BG and GL (after Pearce *et al.*, 1984).

older xenocrystic or derived zircon. It may be noted that detrital zircon geochronological studies of Tethyan Himalayan rocks carried out by Zhu *et al.* (2011) suggesta a Greater Himalayan source for this Neoproterozoic zircon population of the THS. Neoproterozoic ages from the Tethyan Himalaya were also reported by Gehrels *et al.* (2011) and Cao *et al.* (2018). However, the presence of ~550 Ma zircon (Fig. 8b) within the THS indicates that it may have been affected during the final assembly of Gondwana and emplacement of the Palaeozoic Bhaironghati Granite. Petrographic evidences second this view, as an overprint of ductile deformation is evident (Fig. 3b). The complete absence of any younger zircon age peaks also suggests that the THS on the northern part / immediate hanging wall of the JNF is basically the THS, supporting the earlier work of Metcalfe (1993). Pêcher & Scaillet (1989), Pêcher (1991) and Singh (2003) among others have opined that the THS represents a very low-grade metamorphosed part of the GHS, which might have undergone regional folding and/or complete inversion of metamorphic grades. If so, the THS (T2) should have younger syn-Himalayan age imprints (≤55 Ma), similar to the GHS. Although Catlos *et al.* (2020) have obtained one monazite date of ~50 Ma within the THS of the present study area, it could only be correlated with the initial Indo-Eurasian collision and not the major metamorphic or exhumation events of the Greater Himalayan Sequence. This, in turn, again indicates that the JNF

is the actual STD in the Bhagirathi Valley and the THS is the immediate hanging-wall rocks.

6.b. Age and geochemical characteristics of the Bhaironghati Granite: implications for the pre-Himalayan Palaeozoic tectonics and magmatism

The crystallization age we obtained for BG is comparable to, albeit slightly older than, most of the Palaeozoic granites present in the Himalaya. Miller *et al.* (2001) carried out petrogenetic and geochronological studies on the Mandi and Kaplas pluton of Himachal Himalaya and concluded that these plutons formed during the late extensional stage of the Pan-African rifting between ~520 and 610 Ma. Tripathi *et al.* (2012) carried out U–Pb geochronology of zircon from two samples of the Palaeozoic Kinnaur–Kailash Granite and obtained slightly younger ages of ~470 Ma, with a ~20 Ma imprint of syn-Himalayan deformation. Based on their study on the Dalhousie and Dhauladhar Granite of Himachal Himalaya, Dhiman & Singh (2020) envisaged an episode of continental accretion during the amalgamation of Gondwanaland by a reworking of pre-existing Neoproterozoic crust. On the other hand, a study from central Himalaya (Cawood *et al.* 2007) suggests active orogenic setting or the 'North Indian Orogeny' and emplacement of S-type granites at its terminal stages. Geochronological and geochemical studies
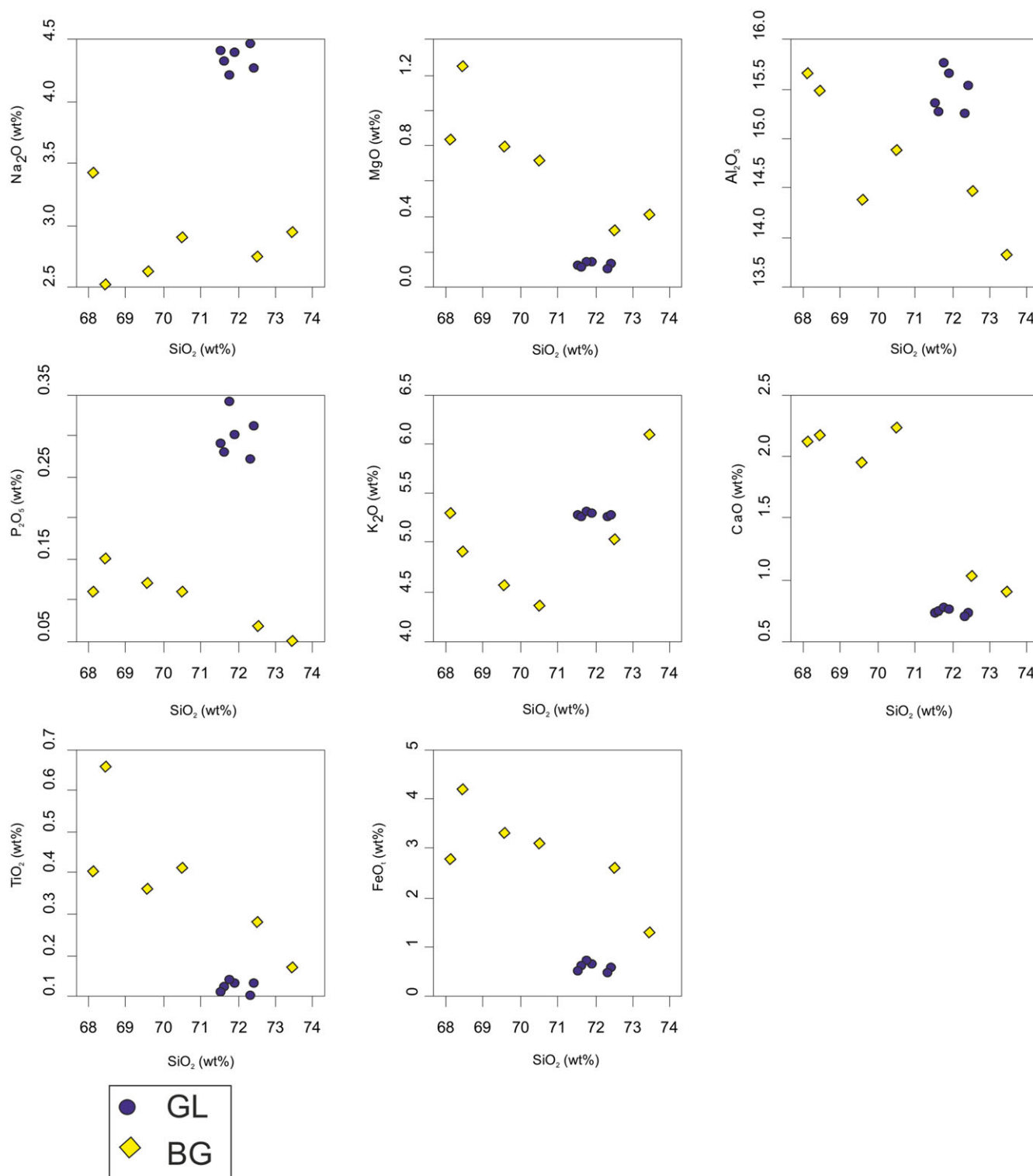
Fig. 6. (Colour online) Harker diagrams depicting multiple plots of SiO_2 vs Na_2O, MgO, Al_2O_3, P_2O_5, K_2O, CaO, TiO_2, FeO_t for BG and GL.

on the Palaeozoic granitic gneisses from the north Himalaya Gneiss Domes and Greater Himalayan Sequence indicate a subduction-induced continental-arc affinity, related to the subduction of the Proto-Tethys (Wang *et al.* 2012).

Our geochemical analyses of the Bhaironghati Granite reveal their peraluminous nature and considerably high FeO + MgO, TiO_2, Ni, Ba, Sr, Th, Zr and Y content at a given SiO_2 content

(Stern *et al.* 1989; Scaillet *et al.* 1995; Singh *et al.* 2003; this study). The decrease in trend of FeO (t) and MgO with rise of SiO_2 also suggests fractionation of mafic minerals. The increasing TiO_2 trend suggests a significant role of biotite and Fe–Ti oxide in the fractionation process. Zircon-hosted biotite fractionation is evident from the tight correlation between Zr and TiO_2 (Clark *et al.* 1993). Zr and P phases show a positive slope in the
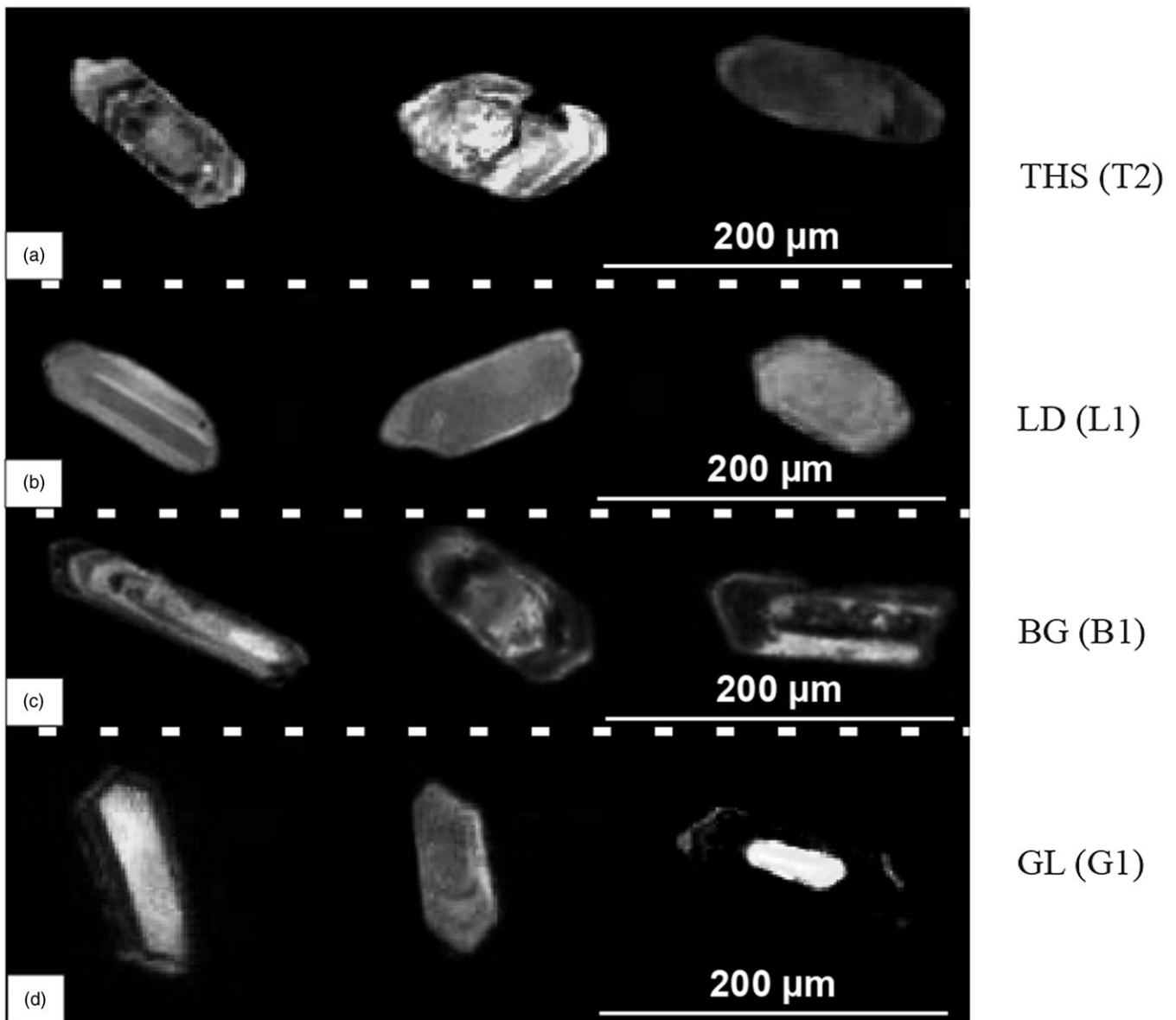
Fig. 7. Cathodoluminescence (CL) images of representative zircon grains reveal different zoning pattern.

primitive-mantle diagrams (Fig. 5a), indicating abundant crystallization of the accessory phases within the BG. The BG is characterized by higher chondrite-normalized REE abundances and high ΣREE, and has a steep slope in LREE patterns (Fig. 5a), revealing that the body is moderately fractionated in HREE with respect to LREE. It also has high La/Yb and Gd/Yb ratios and strong Eu anomaly, indicating fractionation of plagioclase (Fig. 4e, f) (Scaillet *et al.* 1995; Singh *et al.* 2003; this study). Our geochemical analysis clearly shows S-type affinity for the BG (Fig. 5b) and negates any possibility of active/collisional set-up. Therefore, we propose that BG is a vestige of pre-Himalayan Palaeozoic magmatism owing to extensional tectonics probably in a back-arc or rift setting.

Following the extensional collapse of the East African orogen (800–650 Ma), the first stage of tectonic evolution in the early to middle Cambrian (530–500 Ma) led to the assembly of Gondwana. During the assembly, the Proto-Tethyan ocean subducted beneath the Himalayan terrane and Indian craton along the margin of Gondwana that created an active convergent margin

(Lee *et al.* 2000, 2004, 2006; Quigley *et al.* 2006; Cawood *et al.* 2007; Wang *et al.* 2012). Subsequently, rollback of the subducted oceanic lithosphere caused mantle convection and coeval mafic magma underplating, which led to partial melting of the crust and emplacement of early Palaeozoic granites (Miller *et al.* 2001; Visonà *et al.* 2010). The BG has a crystallization age of 514.1 ± 1 Ma (Fig. 9a), which suggests that it emplaced during the initial stages of the Gondwana assembly and the Palaeozoic magmatism occurred in a relatively broad zone of high heat flow and associated crustal melting (Gou *et al.* 2016). Miller *et al.* (2001) suggested that these Paleozoic magmatic rocks formed in a non-arc extensional environment related to collapse of the East African orogeny. Geochronological data from our study along with those from Central Nepal (Gehrels *et al.* 2003, 2006*a*, *b*) suggest that the Palaeozoic magmatism postdates the East African orogeny. Cawood *et al.* (2007) suggested that these Paleozoic magmatic rocks are products of arc magmatism as well as crustal compression. However, our geochemical data reveal that BG was emplaced

Table 3. LA-ICP-MS data for the studied samples (T2, L1, B1, G1)

Sample no.	Isotopic ratios						Age (Ma)						Content (ppm)		
	$^{207}Pb/^{235}U$	2σ	$^{206}Pb/^{238}U$	2σ	$^{207}Pb/^{206}Pb$	2σ	$^{207}Pb/^{235}U$	2σ	$^{206}Pb/^{238}U$	2σ	$^{207}Pb/^{206}Pb$	2σ	U	Th	Pb
T2_40	0.7816	0.0063	0.09531	0.00059	0.05958	0.00017	586.3	3.6	586.8	3.5	588.4	6.1	1033	82	20.09
T2_2	1.193	0.049	0.1224	0.0041	0.07069	0.00061	794	23	744	24	947	18	1436	365	152.9
T2_6	1.158	0.031	0.1229	0.0024	0.06827	0.00048	779	15	747	14	876	15	537	36.9	12.8
T2_28	1.317	0.036	0.1403	0.0034	0.06837	0.00032	851	16	846	19	879.6	9.8	211	56.9	21.34
T2_29	1.341	0.024	0.1416	0.0027	0.06907	0.00024	863	10	854	15	900.8	7.1	496	195	69.3
T2_7	1.334	0.021	0.1424	0.0027	0.06684	0.00058	860.2	9	858	16	835	18	106	44.2	19.36
T2_32	1.471	0.04	0.1445	0.0028	0.07419	0.00092	917	16	870	16	1045	25	483	177	79.5
T2_16	1.516	0.029	0.1457	0.0019	0.07489	0.00074	936	12	877	11	1064	19	315	125.2	57.7
T2_35	1.455	0.019	0.1461	0.0018	0.07192	0.0003	911.5	7.9	881	10	983.3	8.6	632	496	178.8
T2_36	1.4781	0.0075	0.14834	0.00082	0.07258	0.00014	921.4	3.1	891.6	4.6	1002.2	3.9	591	487	176.3
T2_26	1.647	0.019	0.1492	0.0014	0.08033	0.00028	988.3	7.4	896.4	8.1	1205	6.9	788	134.8	61.2
T2_8	1.417	0.024	0.1503	0.0017	0.06881	0.00041	895	10	902.8	9.6	893	12	83	47.4	19.6
T2_31	1.483	0.019	0.1516	0.0031	0.0709	0.00065	924.4	7.7	910	17	953	19	526	190	77.2
T2_12	1.443	0.016	0.1521	0.0016	0.06958	0.0003	907.9	7	912.4	8.8	915.7	8.8	151	127	57.8
T2_18	1.695	0.038	0.1523	0.0045	0.08	0.00087	1006	14	914	25	1196	21	224	146	76.1
T2_5	1.438	0.011	0.1525	0.0015	0.06855	0.00032	904.8	4.7	914.7	8.2	884.7	9.5	412	290	120.4
T2_3	1.5	0.021	0.1556	0.0027	0.07018	0.0005	931.3	8.7	932	15	933	15	427	158	68.3
T2_43	1.87	0.12	0.1558	0.0095	0.08625	0.0006	1063	42	932	53	1343	13	627	417	181.9
T2_11	1.5	0.014	0.1568	0.0015	0.06941	0.0002	930.1	5.7	938.8	8.2	911.8	5.8	143	147	60.5
T2_34	1.535	0.011	0.15812	0.00087	0.07064	0.00018	944.4	4.5	946.3	4.8	946.8	5.1	250	128.3	51.2
T2_4	1.533	0.022	0.1593	0.0028	0.07006	0.00047	944.8	9.1	953	15	929	14	371	175	72.6
T2_1	1.536	0.027	0.1602	0.0026	0.06975	0.00059	944	11	958	14	920	17	361	99.2	44.7
T2_39	1.539	0.017	0.1614	0.0018	0.06947	0.0003	946	7	964	10	912.5	8.8	87.8	104	39.9
T2_45	1.667	0.043	0.1613	0.0036	0.07487	0.0004	997	16	964	20	1064	11	322	154	69.8
T2_15	1.584	0.02	0.1619	0.0021	0.07108	0.00019	963.5	7.9	967	11	959.7	5.4	215.8	88.4	39.8
T2_38	1.566	0.012	0.1636	0.0012	0.06972	0.00031	956.6	4.9	976.5	6.5	919.8	9.2	73.3	82.5	32.5
T2_10	1.764	0.03	0.1675	0.0034	0.07672	0.00043	1032	11	998	19	1115	11	393	182	84.5
T2_9	1.724	0.028	0.1691	0.0029	0.07406	0.00032	1017	10	1007	16	1044.3	9.1	421	81	35.3
T2_27	1.874	0.03	0.1695	0.0027	0.08023	0.00046	1072	11	1010	15	1203	11	423	246.8	116.1
T2_19	1.855	0.031	0.1799	0.0029	0.07502	0.00031	1064	11	1066	16	1068.8	8.4	101.1	115	55.6
T2_33	1.855	0.026	0.1812	0.0025	0.07441	0.0002	1064.7	9.2	1073	14	1052.5	5.5	265	235	107

(*Continued*)

Table 3. (*Continued*)

Sample no.	Isotopic ratios						Age (Ma)						Content (ppm)		
	$^{207}Pb/^{235}U$	2σ	$^{206}Pb/^{238}U$	2σ	$^{207}Pb/^{206}Pb$	2σ	$^{207}Pb/^{235}U$	2σ	$^{206}Pb/^{238}U$	2σ	$^{207}Pb/^{206}Pb$	2σ	U	Th	Pb
T2_23	1.979	0.015	0.183	0.0014	0.07859	0.00012	1108.1	5.2	1083.4	7.4	1162.3	2.9	567	108	66
T2_1	1.915	0.02	0.1869	0.0019	0.07502	0.00029	1085.9	6.9	1104	10	1068.7	7.8	173	133	69.3
T2_30	1.958	0.035	0.1882	0.0036	0.07552	0.0002	1102	13	1111	19	1083.5	5.7	421	229	108
T2_20	1.968	0.025	0.1913	0.0024	0.07498	0.0003	1105.7	8.2	1128	13	1067.8	8.1	74.3	73.2	39.1
T2_14	2.319	0.025	0.1974	0.0021	0.08544	0.00036	1217.9	7.5	1161	11	1326.7	8	385	240	122.6
T2_25	2.378	0.013	0.2056	0.0012	0.08405	0.00036	1235.8	4	1205.5	6.6	1293.4	8.3	428	278	149
T2_13	2.4	0.072	0.2072	0.005	0.0843	0.00058	1239	22	1213	27	1299	14	546	244	136
T2_37	2.767	0.077	0.2125	0.0053	0.09458	0.00028	1345	21	1241	28	1519.7	5.6	410	87.6	43.3
T2_24	2.504	0.069	0.2199	0.0052	0.08216	0.00051	1271	21	1285	27	1249	12	321	302	172
T2_21	2.642	0.067	0.2234	0.0059	0.08638	0.00038	1313	18	1299	31	1346.3	8.3	231	161	92.4
T2_22	2.641	0.053	0.2251	0.0027	0.0863	0.0011	1317	13	1309	14	1343	23	177	99	58.5
T2_44	5.43	0.18	0.2838	0.0081	0.13874	0.00079	1884	29	1609	41	2211.1	9.9	463	587	419
T2_41	5.83	0.15	0.2856	0.0053	0.14854	0.00095	1948	23	1619	27	2329	11	818	477	383
T2_42	8.984	0.095	0.3864	0.0039	0.1687	0.00028	2335.8	9.6	2106	18	2544.8	2.7	362	209	200.6
L1_20	0.644	0.033	0.0753	0.0039	0.06275	0.0003	507	21	468	23	700	10	250	26.58	12.33
L1_18	1.008	0.035	0.1022	0.0039	0.07209	0.00076	706	18	627	23	979	11	593	191	74.3
L1_7	0.893	0.016	0.1066	0.0019	0.06107	0.00017	648.9	8.8	653	11	641.7	5.9	475	197	59.3
L1_8	0.901	0.0056	0.10784	0.0007	0.06094	0.00016	652.2	3	660.2	4.1	637	5.5	361	302	88.4
L1_19	1.023	0.031	0.1162	0.0036	0.06399	0.0002	714	16	708	21	741.3	6.5	595	262	94.6
L1_11	1.246	0.04	0.1192	0.0034	0.07559	0.0003	819	18	725	20	1084	7.9	1044	104	41.3
L1_21	1.393	0.083	0.1282	0.0078	0.07885	0.00043	883	34	776	44	1168	11	551	118	45.7
L1_17	1.472	0.041	0.1298	0.0038	0.0816	0.001	918	17	786	21	1236	24	492	586	247
L1_15	1.406	0.018	0.1406	0.0023	0.07288	0.00026	891.2	7.8	848	13	1010.5	7.1	361	178	71.5
L1_13	1.556	0.031	0.143	0.0023	0.0787	0.001	957	12	861	13	1162	25	429	139	81
L1_23	1.452	0.027	0.1529	0.0034	0.06922	0.00043	910	11	917	19	905	13	407	82.6	40.7
L1_16	1.69	0.041	0.1577	0.0041	0.07813	0.00035	1004	16	944	23	1150	8.9	517	570	261
L1_4	1.513	0.02	0.1582	0.0021	0.06966	0.00024	935.1	8.1	946	12	918	7.1	136	96	41.8
L1_3	1.5162	0.0092	0.1588	0.0012	0.06932	0.00019	936.9	3.7	950.3	6.6	908.1	5.6	238	141.2	61
L1_27	1.566	0.02	0.1593	0.0018	0.07133	0.00039	956.8	8	953	10	967	11	112.6	147.5	67.4
L1_10	1.889	0.054	0.1806	0.0052	0.07742	0.00096	1078	19	1069	28	1129	24	394	133	67.6
L1_26	1.904	0.044	0.184	0.0028	0.07497	0.00067	1082	16	1089	15	1067	18	143	129	65.2

(*Continued*)

Table 3. (*Continued*)

Sample no.	Isotopic ratios						Age (Ma)						Content (ppm)		
	$^{207}Pb/^{235}U$	2σ	$^{206}Pb/^{238}U$	2σ	$^{207}Pb/^{206}Pb$	2σ	$^{207}Pb/^{235}U$	2σ	$^{206}Pb/^{238}U$	2σ	$^{207}Pb/^{206}Pb$	2σ	U	Th	Pb
L1_28	1.93	0.057	0.1849	0.006	0.0759	0.00044	1089	20	1093	33	1092	12	389	46.5	24.8
L1_14	1.937	0.029	0.1864	0.0037	0.07508	0.00044	1093	10	1102	20	1070	12	357	134	71.4
L1_29	2.62	0.12	0.198	0.0059	0.0964	0.0012	1307	32	1164	32	1553	24	434	44.5	28.2
L1_25	2.521	0.097	0.2078	0.0077	0.08767	0.00046	1275	29	1224	43	1375	10	344	258	158
L1_9	2.652	0.028	0.2232	0.0027	0.08654	0.00036	1316.2	8.2	1298	14	1350	7.9	267.1	141	84.8
L1_2	2.601	0.034	0.2279	0.0039	0.08334	0.00044	1300	11	1323	20	1277	10	223	109.8	67.9
L1_1	3.067	0.08	0.2495	0.0072	0.08928	0.00043	1423	20	1435	37	1410.1	9.2	270	147	108.8
L1_22	3.24	0.13	0.251	0.011	0.09317	0.00067	1465	31	1445	56	1491	13	289	135	94
L1_12	3.6	0.12	0.2599	0.0064	0.10109	0.00096	1551	28	1489	33	1643	18	266	319	218
L1_24	7.23	0.25	0.335	0.011	0.15689	0.00037	2135	32	1862	55	2422.4	4	360	84.9	81.3
L1_5	10.36	0.17	0.4376	0.0086	0.17237	0.00049	2469	16	2339	38	2580.7	4.8	188	51.2	57.5
L1_6	10.81	0.13	0.4546	0.0065	0.17389	0.00037	2509	12	2415	29	2595.4	3.6	171	95.4	105.2
B1_1	0.802	0.019	0.07884	0.00043	0.0739	0.0016	598	11	489.2	2.6	1036	42	170	96.4	25.3
B1_2	0.719	0.024	0.0908	0.0031	0.05707	0.00043	550	14	560	19	493	16	253	169	43.1
B1_3	0.6506	0.0071	0.08283	0.00082	0.05685	0.00022	508.7	4.4	513	4.9	485.5	8.4	403.1	136.4	33.37
B1_4	1.42	0.17	0.076	0.0031	0.135	0.012	877	80	472	19	2150	170	224	198	71.6
B1_5	0.627	0.011	0.0764	0.0012	0.05941	0.00016	494.2	6.9	474.7	7.3	582.1	6	1195	182.6	39.6
B1_6	0.73	0.017	0.0898	0.0023	0.05931	0.00024	558	10	555	14	578.2	8.9	1030	157.6	33.43
B1_7	0.6311	0.0092	0.08	0.0013	0.05693	0.00027	496.6	5.7	496.3	7.7	488	10	579	495	118.7
B1_8	0.6539	0.0063	0.08333	0.00091	0.05669	0.00028	510.8	3.9	516	5.4	480	11	228.3	173.6	40.74
B1_9	0.654	0.017	0.083	0.002	0.05726	0.00039	511	11	514	12	501	15	213	164	38.6
B1_10	0.6407	0.0077	0.08175	0.00074	0.05687	0.00034	502.6	4.8	506.5	4.4	486	13	107.7	83.7	20.12
B1_11	0.652	0.011	0.0767	0.0016	0.06184	0.00032	511	7.3	478	9.1	668	11	1015	74.4	20.1
B1_12	0.666	0.018	0.0826	0.0018	0.0584	0.00057	518	11	511	11	544	21	284	153.8	37.7
B1_13	0.512	0.019	0.0616	0.0023	0.05991	0.00013	419	13	385	14	600.5	4.9	5250	3230	459
B1_14	0.684	0.012	0.0872	0.0017	0.05634	0.00023	528.8	7.4	539.1	9.9	465.6	9.2	281	138.8	33.6
B1_15	0.666	0.018	0.0832	0.0024	0.05791	0.0006	517	11	515	14	525	22	228	170	41.8
B1_16	0.643	0.012	0.0822	0.0018	0.05672	0.00026	503.7	7.4	509	11	480	10	680	299	65.8
B1_17	0.6085	0.007	0.07805	0.00052	0.05676	0.00029	482.6	4.4	484.4	3.1	482	11	211.5	145.4	34.03
B1_18	1.51	0.14	0.0878	0.0019	0.1223	0.0096	923	59	542	11	1950	150	122.5	91.8	38.8
B1_19	0.65	0.024	0.0816	0.0031	0.05733	0.00043	508	14	506	18	504	16	760	900	108

(*Continued*)

Table 3. (*Continued*)

Sample no.	Isotopic ratios						Age (Ma)						Content (ppm)		
	$^{207}Pb/^{235}U$	2σ	$^{206}Pb/^{238}U$	2σ	$^{207}Pb/^{206}Pb$	2σ	$^{207}Pb/^{235}U$	2σ	$^{206}Pb/^{238}U$	2σ	$^{207}Pb/^{206}Pb$	2σ	U	Th	Pb
B1_20	0.6042	0.005	0.07737	0.0007	0.0567	0.00025	479.8	3.2	480.4	4.2	479.4	9.6	283.7	173.7	38.9
B1_21	0.669	0.012	0.0825	0.0012	0.0597	0.0018	519.7	7.5	511.2	7	559	34	449	676	167
B1_22	0.657	0.039	0.0763	0.0034	0.06158	0.00084	510	24	473	21	657	28	1040	410	28.3
B1_23	0.679	0.015	0.0849	0.0024	0.05711	0.00047	525.9	9.4	527	14	495	18	249	169.6	39.6
B1_24	0.628	0.011	0.0812	0.0012	0.05652	0.00023	494.7	6.6	503.2	7.3	472.8	9.1	549	360	78
B1_25	0.634	0.016	0.0794	0.002	0.05759	0.00049	498.3	9.6	493	12	513	18	760	428	100.7
B1_26	1.394	0.019	0.1472	0.0023	0.06876	0.00034	888.1	8.9	885	13	891	10	401	246	99.7
B1_27	0.611	0.017	0.0754	0.0013	0.05931	0.00061	486	10	468.9	7.9	577	23	1049	471	102.7
B1_28	0.66	0.0072	0.08343	0.00096	0.05729	0.00027	514.5	4.4	516.5	5.7	502	11	202	103.9	25.5
B1_29	0.653	0.019	0.0828	0.0027	0.05697	0.00043	510	12	515	15	490	17	327	204	51.6
B1_30	1.159	0.062	0.0741	0.0012	0.1127	0.0043	779	29	460.7	7	1853	73	140.1	279.8	30.5
B1_31	0.6222	0.0049	0.06164	0.00087	0.07234	0.00067	491.2	3.1	385.6	5.3	995	19	148.5	210.9	30.1
B1_32	0.674	0.043	0.084	0.0043	0.0591	0.0013	520	24	520	26	566	44	536	263	66.4
B1_33	1.75	0.15	0.1423	0.0091	0.0884	0.0027	1025	54	857	51	1388	58	270	77	20.9
B1_34	0.5829	0.0051	0.07421	0.00047	0.05692	0.00026	466.3	3.2	461.5	2.8	488	10	335	209	47.67
B1_35	0.586	0.014	0.0749	0.0011	0.05667	0.0006	468.5	8.9	465.5	6.5	478	23	241.2	154.3	36.66
B1_36	3.934	0.088	0.2466	0.0057	0.11404	0.00053	1619	18	1420	29	1864.5	8.5	295	199	148
B1_37	0.5184	0.0083	0.0604	0.0012	0.06182	0.00061	423.9	5.5	378.2	7.3	666	21	355	157.2	28.4
B1_38	0.67	0.015	0.0793	0.0018	0.06127	0.00035	520.8	9.1	492	11	648	12	617	174.4	37.7
G1_1	1.107	0.01	0.1235	0.0012	0.06496	0.00033	756.7	4.9	750.8	7.1	729.4	5.8	200	199.9	68
G1_2	0.0578	0.0067	0.003308	0.000066	0.125	0.012	56.8	6.3	21.29	0.42	720	110	2.21E+04	387	139
G1_3	0.03049	0.00093	0.003385	0.000044	0.0656	0.0016	30.49	0.92	21.78	0.28	321	18	20670	230.8	32.8
G1_4	0.336	0.026	0.00558	0.00021	0.445	0.016	291	20	35.9	1.3	3930	260	3.03E+04	770	1520
G1_5	0.1172	0.0094	0.00693	0.00011	0.123	0.011	112.5	8.5	44.54	0.7	952	53	4440	205	91
G1_6	0.0577	0.0026	0.00422	0.00012	0.0982	0.0035	56.9	2.5	27.13	0.78	154	12	12960	1050	80
G1_7	2.07	0.13	0.031	0.0018	0.493	0.013	1137	43	197	12	1180	160	1960	1530	817
G1_8	0.0223	0.0011	0.003018	0.000061	0.0538	0.0017	22.4	1.1	19.42	0.39	122	21	23990	260	13.8
G1_9	0.02899	0.0007	0.003882	0.000097	0.05436	0.00078	29.01	0.69	24.98	0.62	115	23	10390	129.4	7.7
G1_10	0.2575	0.002	0.03151	0.00025	0.05934	0.00013	232.6	1.6	200	1.5	161	15	3435	33.06	2.5
G1_11	0.738	0.057	0.0476	0.0036	0.11377	0.00035	559	34	299	22	1215	51	2520	63	37.3
G1_12	4.472	0.089	0.2691	0.0055	0.12159	0.00072	1725	17	1536	28	1737	22	471	85.9	73

Table 3. (*Continued*)

Sample no.	Isotopic ratios						Age (Ma)						Content (ppm)		
	^{207}Pb/^{235}U	2σ	^{206}Pb/^{238}U	2σ	^{207}Pb/^{206}Pb	2σ	^{207}Pb/^{235}U	2σ	^{206}Pb/^{238}U	2σ	^{207}Pb/^{206}Pb	2σ	U	Th	Pb
G1_13	0.271	0.025	0.0207	0.0016	0.0934	0.0027	241	20	132	10	493	80	4300	301	51.4
G1_14	0.374	0.056	0.01678	0.00086	0.176	0.03	314	39	107.2	5.5	647	71	4260	840	239
G1_15	0.1031	0.0071	0.012961	0.000097	0.0582	0.0041	99.5	6.5	83.01	0.62	138	10	1411	500	31.5
G1_16	0.213	0.012	0.0195	0.0014	0.0769	0.0031	195.6	9.7	124.4	8.7	710	150	5080	238	55.4
G1_17	1.046	0.023	0.0665	0.0017	0.1136	0.0013	726	12	415	10	931	40	1292	162.9	70.8
G1_18	0.0292	0.0031	0.002997	0.000057	0.0717	0.0073	29.2	3	19.29	0.37	295	84	2.97E+04	321	48
G1_19	1.194	0.024	0.1105	0.0012	0.0781	0.0024	797	11	675.4	7	772	26	952	453.3	161.1
G1_20	0.195	0.063	0.00332	0.00043	0.395	0.08	176	51	21.4	2.8	224	38	2.55E+04	9.20E+03	830
G1_21	0.0716	0.0064	0.0035	0.00013	0.149	0.015	70.2	6	22.55	0.86	270	45	9.80E+03	1410	108
G1_22	0.084	0.011	0.00352	0.00017	0.178	0.021	81	10	22.6	1.1	510	130	4020	202	50
G1_23	0.15	0.012	0.0175	0.0013	0.06202	0.00056	141	10	111.6	8.2	507	24	2290	243	55.8
G1_24	0.1397	0.006	0.0137	0.00038	0.0736	0.0021	132.7	5.4	87.7	2.4	506	14	820	100.9	23.46
G1_25	0.091	0.046	0.00393	0.0003	0.159	0.069	87	41	25.3	1.9	445	62	11530	630	150
G1_26	0.159	0.014	0.0169	0.0013	0.065	0.0015	149	12	108.3	8.6	210	25	5310	599	53.6
G1_27	0.0566	0.0092	0.00318	0.00012	0.127	0.017	55.6	8.7	20.48	0.74	790	230	3.27E+04	700	202
G1_28	0.26	0.016	0.0315	0.0019	0.05938	0.00031	233	13	200	12	77	13	1.10E+04	280	7
G1_29	0.2031	0.0082	0.01972	0.00043	0.0731	0.0023	187.6	6.9	125.9	2.7	985	88	1146	36.4	16.5
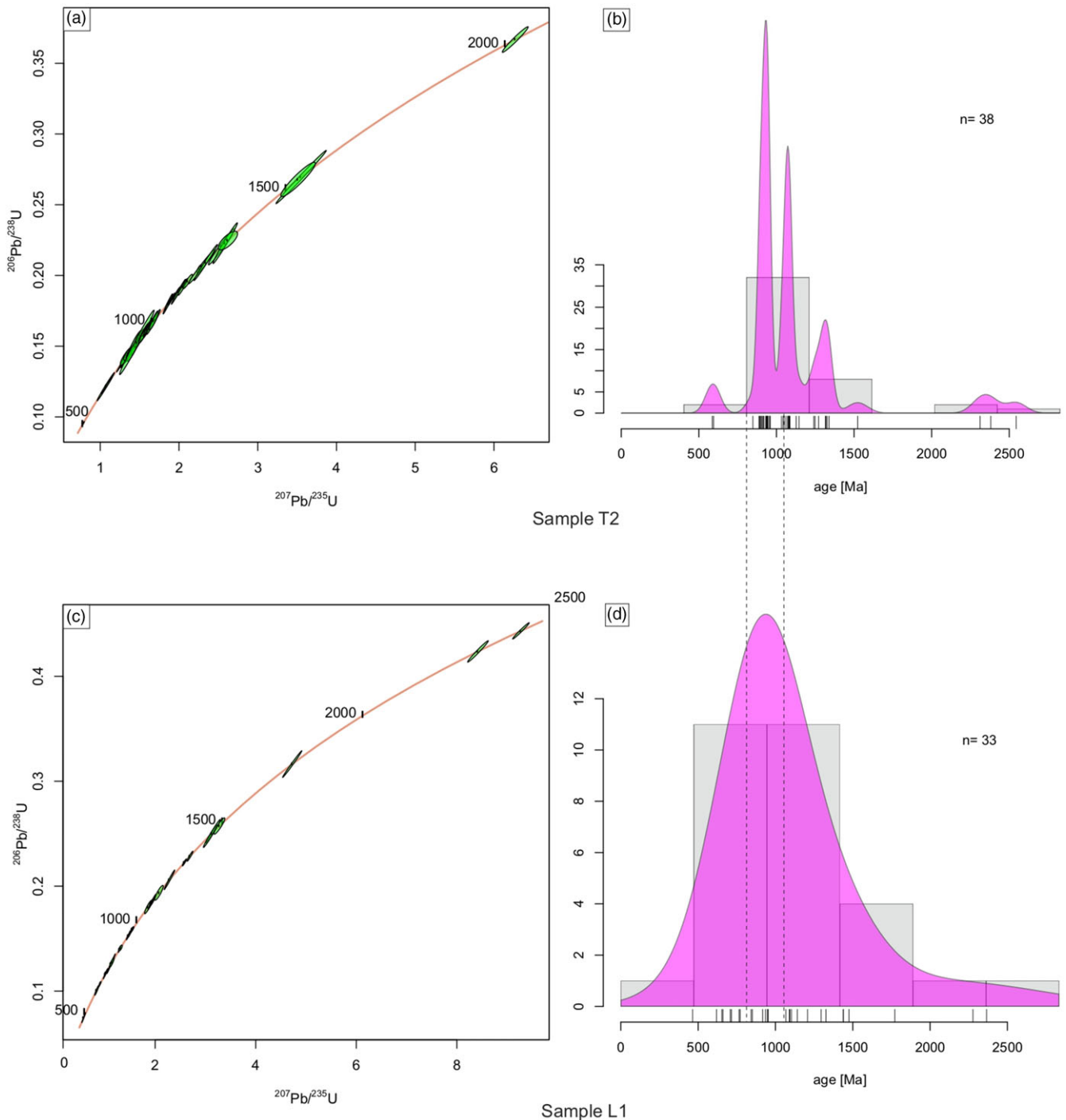
Fig. 8. (Colour online) Zircon U–Pb plots for samples T2 and L1. (a) A Wetherill concordia diagram of sample T2 exhibits the entire age spectrum between ~2500 and 500 Ma, along with the Th/U ratio of each point. (b) A kernel density estimation of the concordant ages reveals the most prominent age peak at ~1000 Ma. (c) A Wetherill concordia diagram of sample L1 exhibits the entire age spectrum between ~2500 and 500 Ma, along with the Th/U ratio of each point. (d) A kernel density estimation of the concordant ages reveals striking similarities in the age peaks between samples T2 and L1, with the most prominent age peak at ~1000 Ma.

in a post-collisional within-plate back-arc tectonic setting (Fig. 5b). It can be argued that, following the initial mafic magma underplating and generation of an initial magmatic arc, the high heat flow and eventual melting of the crust led to formation of a back-arc environment between ~530 and 500 Ma, which triggered the emplacement of BG and other equivalent Palaeozoic magmatic rocks. From the Rb/Sr vs Ba diagram (Fig. 4d; Inger & Harris,

1993), it can be inferred that the BG is a product of biotite-dehydration melting, which suggests that mafic magma was emplaced below the lower crust to elevate the crustal geotherms ($T \sim 660–710$ °C). Such a condition is suitable for *in situ* partial melting of biotite-rich metapelites (Gou *et al.* 2016). This is further supported by the study of Visonà & Lombardo (2002) and Wang *et al.* (2012) who suggested that the Palaeozoic granites resulted
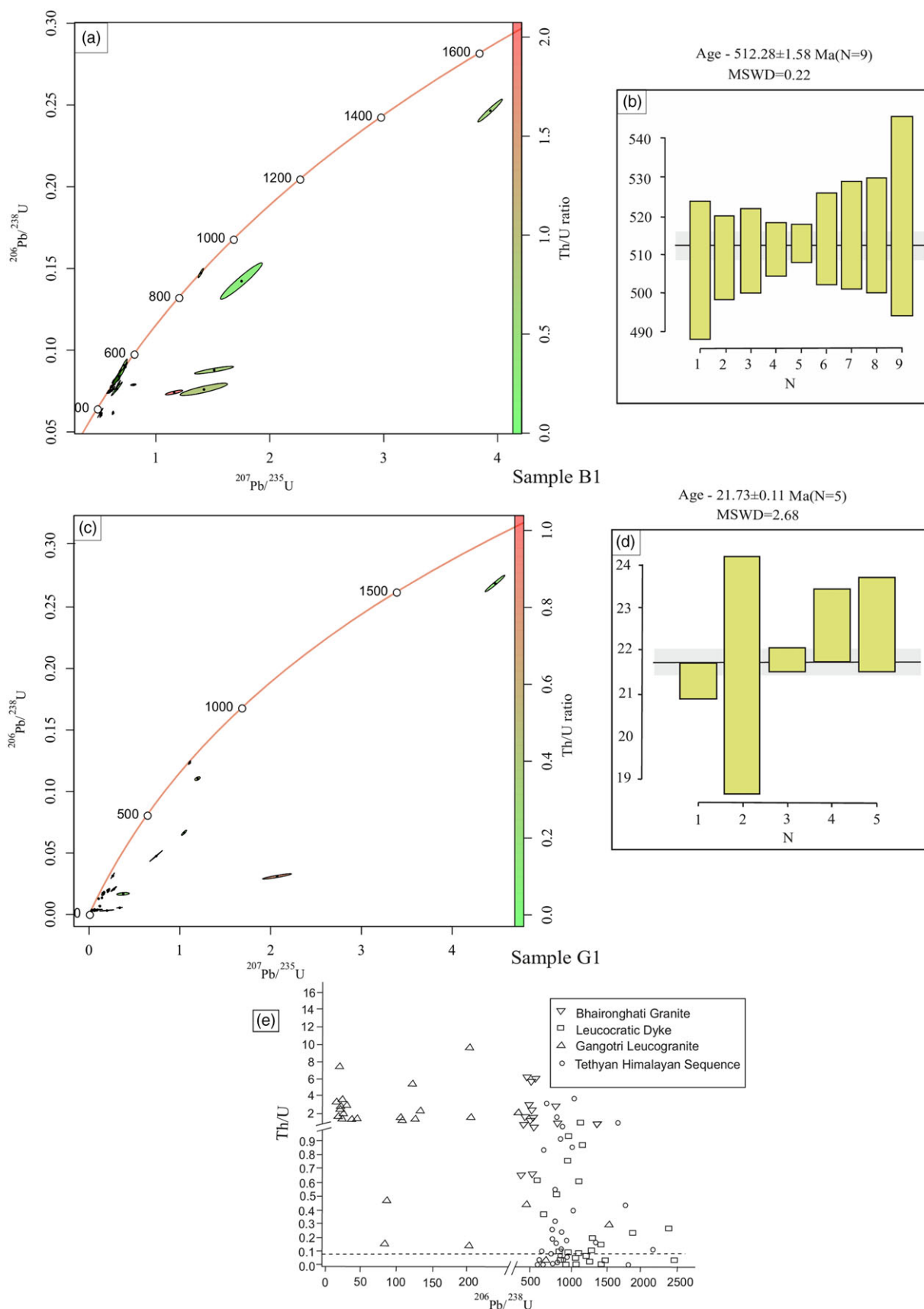
Fig. 9. (Colour online) Zircon U–Pb plots for samples B1 and G1. (a) A Wetherill concordia diagram along with the Th/U ratio of sample B1 reveals that the majority of the spot ages are concentrated near ~500 Ma. (b) The weighted mean average age is calculated from the concordant spot ages that are concentrated near ~500 Ma. (c) A Wetherill concordia diagram of sample G1 reveals that the majority of the spot ages are concentrated near ~20 Ma. (d) The weighted mean average age is calculated from the concordant spot ages that are concentrated near ~20 Ma. (e) Th/U ratio vs $^{206}Pb/^{238}U$ age of GL, BG, leucocratic dyke and THS.
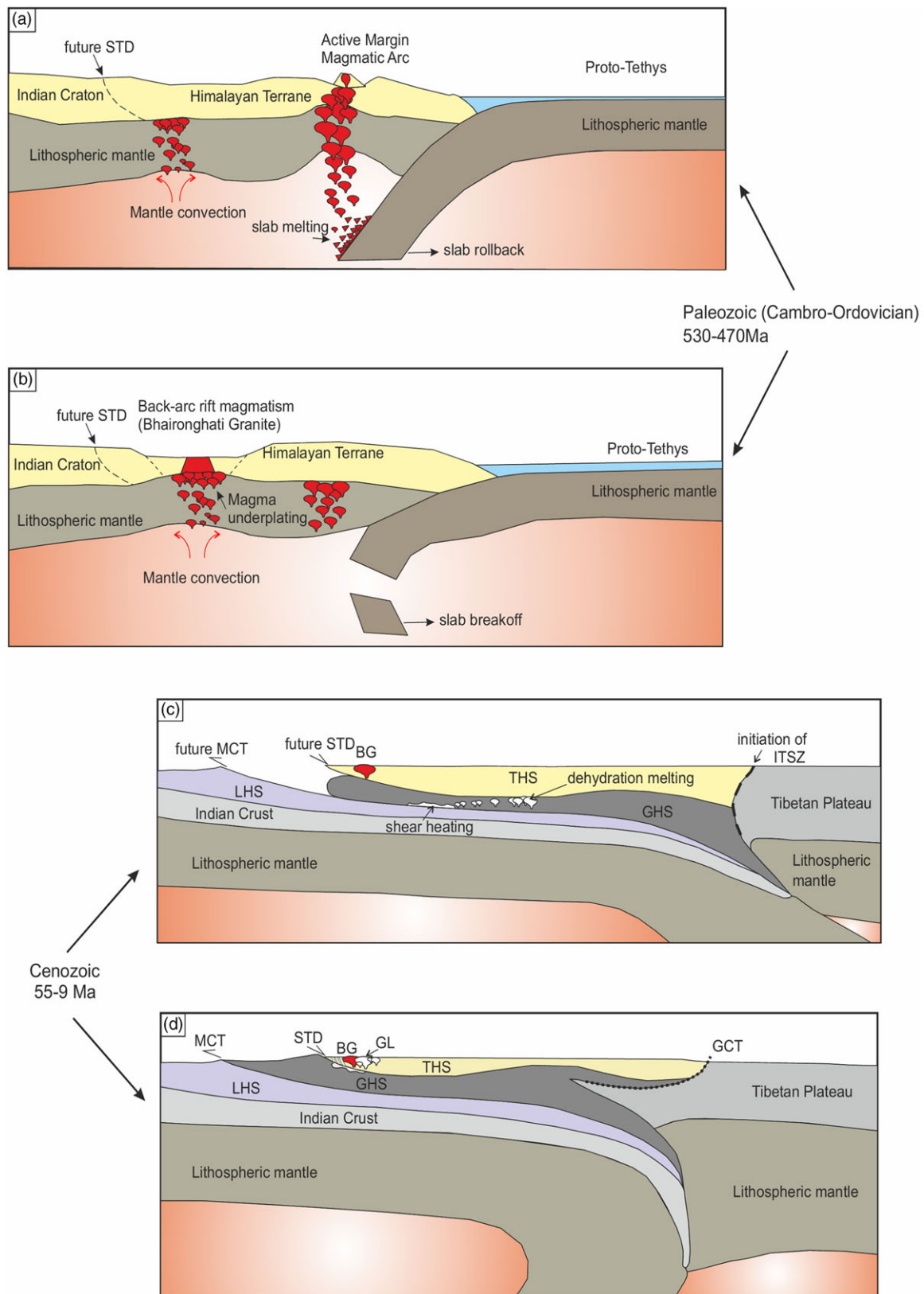
Fig. 10. (Colour online) Cartoon showing different stages of orogeny build-up and related magmatism involved in the pre- and syn-Himalayan stages. (a, b) Stages of pre-Himalayan tectonic evolution with involvement of back-arc rift (S-type) magmatism in the Palaeozoic. Following the initial mafic magma underplating and generation of initial magmatic arc, high heat flow and eventual melting of the crust led to formation of a back-arc environment between ~530 and 500 Ma, which triggered the emplacement of BG and other equivalent Palaeozoic magmatic rocks (modified after Guo & Wilson, 2012). (c, d) Cenozoic deformation, magmatism and related metamorphism in exhumation of the GHS and related GHL during the Himalayan orogeny. The Gangotri Leucogranite (GL) is a result of muscovite-dehydration melting of the lower crust, with the possible reason for generation and emplacement of this silicic melt being flexural bending in relation to the steepening of the subducted Indian lithosphere, which caused reheating of the Indian lithosphere below Himalaya (modified after King *et al.* 2011; Gou *et al.* 2016).

from melting of the crust with heat input from the underplated mafic magmas and were formed in a back-arc environment close to the continental volcanic arc (Fig. 10 a, b).

Pre-Himalayan Palaeozoic deformation and metamorphism have been studied in some parts of the Higher Himalaya, especially in the Nepal Himalaya (Gehrels *et al.* 2006*a*, *b*). These studies suggest deformation and metamorphism of pelitic rocks in Palaeozoic times and syn- to post-deformation emplacement of Palaeozoic granites. In the present study area, the BG is associated with the low-grade THS or the Harshil Group of rocks with a tectonic/mylonitized contact. U–Pb geochronology suggests an imprint of ~550 Ma ages within the THS (probably during emplacement of BG), while BG is Palaeozoic with very little inherited zircon of Paleproterozoic and Neoproterozoic ages. We infer that the ~550 Ma zircon population within the THS indicates that, as a host body, the THS may have been affected by the Palaeozoic magmatism and emplacement of the BG, at least along the periphery of the BG.

6.c. Age and geochemical characteristics of the Gangotri Leucogranite: implications for the Cenozoic tectonics and magmatism

The Cenozoic Leucogranites are found along-strike the entire Himalayan range, occurring generally on the footwall or the immediate hanging-wall side of the STD and within the THS. These leucogranites vary in age from ~30 Ma to ~7 Ma (Yin, 2006 and references therein; Sen *et al.* 2015 and references therein). They generally either form a discontinuous chain of sills and dykes or are present as laccoliths. Subsequently, they exhumed and were exposed adjacent to the STD, separating the GHS from the low-grade to pristine THS (Scaillet *et al.* 1990, 1996; Harris & Massey, 1994; Searle, 1999).

Our geochemical analyses reveal that GL is a product of melting of the upper crust. The Gangotri Leucogranites have considerably high Al_2O_3, Na_2O, P_2O_5 and Rb contents, and lower Fe_2O_3, MgO, CaO, K_2O, TiO_2, Ba, Sr, Th, Zr and Y contents at a fixed SiO_2 content which signify lower abundance of mafic minerals. Low FeO (t) and MgO indicate their insignificant contribution in the crystallization and fractionation processes (Figs 5a, 6) (Scaillet *et al.* 1996; Singh *et al.* 2003; present study). The P_2O_5 range at a given SiO_2 content is very narrow, suggesting a negligible to very low amount of apatite crystallization (Fig. 6; Stern *et al.* 1989; Manickavasangam *et al.* 1999). Similarly, the primitive-mantle normalized diagrams (Fig. 5a) reveal a negative Zr anomaly, indicating a moderate degree of partial melting of the felsic source. Considering the Rb/Sr vs Ba plots (Fig. 4d), it is inferred that the GL formed as a result of fluid-absent incongruent partial melting by muscovite-dehydration processes. Most of the Greater Himalayan Leucogranites along-strike the Himalaya are a result of muscovite vapour-absent melting reactions. This process generally requires a decrease in pressure conditions which could have been obtained during rapid exhumation and subsequent erosional processes (Clemens & Vielzeuf, 1987; Harris & Massey, 1994; Scaillet *et al.* 1996; Searle, 1999; Guo & Wilson, 2012; Gou *et al.* 2016) (Figs 4d and 5a).

U–Pb dating of zircon from a representative sample of GL (sample G1) yielded a crystallization age of 21.73 ± 0.011 Ma. This age is contemporaneous with most of the leucogranites from the Western Himalaya (cf. Yin, 2006 and references therein; Sen *et al.* 2015 and references therein; Horton *et al.* 2015; Weinberg, 2016; Montemagni *et al.* 2020).

Previous studies have defined the leucogranite magmatism as a product of intense crustal melting related to the N–S extension-induced normal fault system (JNF/STD) (Guillot & Le Fort, 1995; Carosi *et al.* 1998; Zhang *et al.* 2004, 2005; Xu *et al.* 2006). The leucogranites are differentiated as GHL (Greater Himalayan Leucogranites) and THL (Tethyan Himalayan Leucogranites) on the basis of their geochemical and isotopic characteristics (King *et al.* 2011; Guo & Wilson, 2012). These leucogranites were emplaced from south (GHL) to north (THL) following the progressive northward thrusting of the Indian subcontinent following the initiation of India–Asia collision along with two-component mixing in the source region between the GHS and fluids derived from underlying LHS. Gou *et al.* (2016) predicted a ~15–20 % melt production for the pelitic schists and orthogneisses of the GHS. Melt thus produced was sufficient for formation of GHL and THL. GHL is mostly tourmaline–muscovite leucogranites, whereas THL is a two-mica leucogranite. This suggests that the GHL and THL have different crystallization temperatures and were the product of separate dehydration melting reactions.

Our study reveals that the Gangotri Leucogranites have high Rb/Sr ratios, negative correlation of Ba content with the Rb/Sr ratios, low Sr/Ba ratios and distinct Eu anomalies (Fig. 5a; Table 2). Hence, these leucogranites are the product of muscovite-dehydration melting, and can be classified as the GHL (Scaillet *et al.* 1995; Singh, 2018; present study). According to Guo & Wilson (2012), underthrusting of the Indian subcontinent during post-India–Asia collision (~55 Ma) resulted in metasomatism of the GHS sequence with mixing of fluids from LHS that led to generation of leucogranite magmas with phases of decompression and reheating (25–9 Ma). Flexural bending in relation to the steepening of the subducted Indian lithosphere caused reheating of the Indian lithosphere below the Himalaya due to upwelling of asthenospheric mantle. This formed a zone of N–S extension (JNF/STD) along which the Cenozoic leucogranites were emplaced (Fig. 10c, d). Furthermore, the devolatilizing muscovite reactions might have reduced the viscosity by producing a moderate percentage of *in situ* partial melt. This is evident on the initiation of magmatism and later exhumation-controlled development of the migmatite zone at higher structural heights of the GHS and within many parts of the Himalayan hinterland (Patiño Douce & Harris, 1998; Gou *et al.* 2016; Singh, 2018).

6.d. Significances of concentration of Th and U and their ratios

The concentrations of heat-producing elements (U, Th and K) have a significant effect on the magmatic and tectono-metamorphic evolution of the crust. With the onset of crustal anataxis, the growth, breakdown and partitioning of Th and U into accessory minerals affect the crustal differentiation process. The GL and BG are high-*T* melt products, and equilibrium concentrations of Th, U, K and LREE in these rock bodies provide a hint as to the chemical composition of the lower and middle crust from which the melt evolved (Villaseca *et al.* 2003; Yakymchuk *et al.* 2018; Yakymchuk & Brown, 2019). From the geochemical analysis of GL and BG and the low-grade sedimentary THS, it is inferred that the distribution of LREE, Zr and P in the rock-forming minerals during crustal melting and anataxis may significantly affect the partition of heat-producing elements (Bea, 2012). Geochemical analysis (Figs 4, 5) and Th/U ratios of sedimentary THS and GL and BG suggest concentration of K and U decreases with increasing

temperature, whereas concentration of Th slowly increases (Fig. 9c). Furthermore, it is observed that most of the zircon analyses from GL and BG have Th/U ~1 or >1; whereas Th/U ratio < 1 in zircon from THS and THS-hosted leucocratic dyke. It can be inferred that GL and BG are completely hosted by igneous zircon and any kind of kinetic restrictions on dissolution of Th and U, or distribution coefficients between zircon, apatite and melt, may significantly affect the partitioning of Th and U into melt production. From our observations, it can be argued that the relative increase in Th/U ratio for GL and BG may either be caused by preferential breakdown of U-rich accessory minerals, or precipitation of high Th/U accessory minerals in the source melt during emplacement. Furthermore, the retention of Th and U by GL and BG, both mid-crustal melt derivatives, suggest that retention of heat-producing elements may be responsible for the generation of radiogenic heat during crustal melting, as heat provided by lithospheric mantle is limited and insufficient to cause melting and exhumation.

6.e. Relationship between leucocratic dykes and the Gangotri Leucogranite

The batch of leucocratic dykes (L1), appearing on the immediate hanging wall of the JNF in the Tethyan metasedimentary rocks (THS), is different from the GL in terms of itsmineralogy and texture. Earlier workers suggested that this set of leucocratic dykes is characteristically a part of the Gangotri Leucogranite as it has almost the same mineralogy and texture. It is also suggested that these dykes are more refracted in nature, representing an over-saturated part of the same melt upwelling (Scaillet *et al.* 1995; Sorkhabi *et al.* 1999; Searle, 1999; Singh *et al.* 2003). Our study shows that the leucocratic dykes are mineralogically different than the GL as they contain a small amount of sillimanite with large blebs of tourmaline along with over-saturation of silica. Geochemical analyses of the leucocratic dykes associated with the THS host rock suggest that their composition is highly silicic ($SiO_2 = 74.44–75.6$ wt %), and sodic ($Na_2O = 5.54–5.6$ wt %). Moderate enrichment of light REE and strong Eu anomaly characterize these dykes (Figs 5, 6; Table 2). These leucocratic dykes have lower ΣREE, lower CaO, K_2O and equivalent Fe_2O_3 contents. The leucocratic dykes also have very low Sr, Ba, Zr contents and also less Sr/Y, Zr/Hf ratios, but high Rb concentrations and Rb/Sr ratios along with their highly peraluminous nature (Fig. 5). The Rb/Sr vs Ba (Fig. 4d) suggests that the dykes are a result of muscovite-vapour present reaction conditions. The probable reason is that K-feldspar from the immediate footwall of the JNF along with quartz and plagioclase from the THS host rock body might have participated in the production of the melt in the water-saturated and vapour-present conditions (Scaillet *et al.* 1995). The dehydration-melting solidus for muscovite-bearing rocks has a smaller dP/dT slope. Hence, a protolith of muscovite-bearing schist undergoes decompression melting more readily, suggesting that muscovite is a deep crustal H_2O reservoir (Patiño Douce, 1997; Patiño Douce & Harris, 1998; Patiño Douce & McCarthy, 1998). Dehydration melting of metapelites during adiabatic compression (6–8.5 kbar, 750–850 °C) is attributed to the generation of leucogranitic magmas in the Himalaya.

Zircon U–Pb LA-MC-ICP-MS geochronological analyses indicate that the zircon hosted within these leucocratic dykes is mostly inherited. Geochronological data from sample L1 reveal a wide scattering of age between ~550 and 1700 Ma, with the most prominent peak at 930 Ma (Fig. 8b). Such a striking similarity in the

age-peaks from both samples T2 and L1 suggests that the zircon of L1 is basically part of the THS host-rock body that may have been incorporated into the melt as a result of wall-rock assimilation. The melt, from which this set of leucocratic dykes was produced, was too refracted to produce any zircon from the melt during the formation of the dykes.

Furthermore, regarding the possible sources of the leucocratic dykes on the immediate hanging wall of the JNF, it can be argued that the Bhaironghati granite cannot be one as it shows no signature of deformation or partial melting. The THS, despite being the host rock, is unlikely to be a source, as its metamorphic grade is too low to produce partial melts and finally over-saturated leucocratic dykes. Ascent and emplacement of granitic rocks, especially a highly silicic leucocratic variety like these dykes, will require the assistance of regional deformation that would create space for the highly viscous leucocratic melt to ascend and emplace (Rosenberg *et al.* 1995; Vigneresse *et al.* 1999). We opine that these leucocratic dykes are highly refracted parts of the Gangotri Leucogranite that migrated and emplaced along extensional fault zones related to the JNF/STD. Since the BG is a massive and compact pluton devoid of any structural anisotropy, this highly viscous leucocratic melt could not penetrate the BG pluton and was only observed within the weaker and foliated THS.

7. Conclusions

1. The Jhala Normal Fault (JNF)/STD marks the onset of the THS and shows top-to-the-NE extensional shear with some amount of top-to-the-S compressive shear, which appears to be older.
2. The Bhaironghati Granite (BG) is an S-type two-mica granite and a product of pre-Himalayan Palaeozoic magmatism owing to extensional tectonics in a back-arc or rift setting.
3. The Gangotri Leucogranite (GL) is a result of muscovite-dehydration melting of the lower crust. The possible reason for generation and emplacement of this silicic melt may be flexural bending in relation to the steepening of the subducted Indian lithosphere which caused reheating of the Indian lithosphere below Himalayan orogen.
4. The leucocratic dykes present within the THS are highly refracted parts of the Gangotri Leucogranite that migrated and emplaced along extensional fault zones related to the JNF/STD.

References

Auden JB (1949) Tehri Garhwal and British Garhwal. *Recordings of the Geological Survey of India* **76**, 74–8.

Bea F (2012) The sources of energy for crustal melting and the geochemistry of heat-producing elements. *Lithos* **153**, 278–91. doi: 10.1016/j.lithos.2012.01.017.

Boynton WV (1984) Geochemistry of rare earth elements: mateorite studies. In *Rare Earth Element Geochemistry* (ed. P Henderson), pp. 63–114. New York: Elsevier.

Cao H, Huang Y, Li G, Zhang L, Wu J, Dong L, Dai Z and Lu L (2018) Late Triassic sedimentary records in the northern Tethyan Himalaya: tectonic link with Greater India. *Geoscience Frontiers* 9, 273–91.

Carosi R, Lombardo B, Molli G, Musumeci G and Pertusati, PC (1998) The south Tibetan detachment system in the Rongbuk valley, Everest region: deformation features and geological implications. *Journal of Asian Earth Sciences*, 16, 299–311.

Catlos EJ, Perez TJ, Lovera OM, Dubey CS, Schmitt AK and Etzel TM (2020) High-Resolution P-T-Time Paths across Himalayan faults exposed along the Bhagirathi Transect NW India: implications for the construction of the Himalayan Orogen and ongoing deformation. *Geochemistry, Geophysics, Geosystems* 21, e2020GC009353.

Cawood PA, Johnson MRW and Nemchin AA (2007) Early Paleozoic orogenesis along the Indian margin of Gondwana: tectonic response to Gondwana assembly. *Earth and Planetary Science Letters* 255, 70–84.

Chang Z, Vervoort JD, McClelland WC and Knaack C (2006) U-Pb zircon dating by LA-ICP-MS. *Geochemistry, Geophysics, Geosystems* 7, Q05009. doi: 10.1029/2005GC001100.

Clark DB, McDonald MA, Reynold PH and Longstaffe FJ (1993) Leucogranites in the Lachlan fold belt. *Transactions of the Royal Society of Edinburgh* 83, 1–26.

Clemens JD and Vielzeuf D (1987) Constraints on magma melting and production in the crust. *Earth and Planetary Science Letters* 86, 287–306.

Davidson C, Grujic DE, Hollister LS and Schmid SM (1997) Metamorphic reactions related to decompression and synkinematic intrusion of leucogranite, High Himalayan Crystallines, Bhutan. *Journal of Metamorphic Geology* 15, 593–612.

Dhiman R and Singh S (2020) Neoproterozoic and Cambro-Ordovician magmatism: episodic growth and reworking of continental crust, Himachal Himalaya, India. *International Geology Review* 63.doi: 10.1080/00206814.2020.1716399.

El Bouseily AM and El Sokkary AA (1975) The relation between Rb, Ba and Sr in granitic rocks. *Chemical Geology* 16, 207–19. doi: 10.1016/0009-2541(75)90029-7.

Frost BR, Barnes CG, Collins WJ, Arculus RJ, Ellis DJ and Frost CD (2001) A geochemical classification for granitic rocks. *Journal of Petrology* 42, 2033–48.

Gansser A (1964) *Geology of the Himalayas*. London: Interscience, 289 pp.

Garzanti E, Casnedi R and Jadoul F (1986) Sedimentary evidence of a Cambro-Ordovician orogenic event in the Northwestern Himalaya. *Sedimentary Geology* 48, 237–65.

Gehrels GE, DeCelles PG, Martin A, Ojha TP, Pinhassi G and Upreti BN (2003) Initiation of the Himalayan orogen as an early Paleozoic thin-skinned thrust belt. *GSA Today* 13, 4–9.

Gehrels GE, DeCelles PG, Ojha TP and Upreti BN (2006a) Geological and U–Pb geo- chronologic evidence for early Paleozoic tectonism in the Dadeldhura thrust sheet, far-west Nepal Himalaya. *Journal of Asian Earth Sciences* 28, 385–408.

Gehrels GE, DeCelles PG, Ojha TP and Upreti BN (2006b) Geologic and U–Th–Pb geo- chronologic evidence for early Paleozoic tectonism in the Kathmandu thrust sheet, central Nepal Himalaya. *Geological Society of American Bulletin* 118, 185–98.

Gehrels GE, Kapp P, DeCelles PJ, Pullen A, Blakey R, Weislogel A, Ding L, Guynn J, Martin A, McQuarrie N and Yin A (2011) Detrital zircon geochronology of pre-Tertiary strata in the Tibetan-Himalayan orogen. *Tectonics* 30, TC5016. doi: 10.1029/2011TC002868.

Gehrels GE, Valencia V and Ruiz J (2008) Enhanced precision, accuracy, efficiency, and spatial resolution of U-Pb ages by laser ablation-multicollector-inductively coupled plasma-mass spectrometry. *Geochemistry, Geophysics, Geosystems* 9, Q03017. doi: 10.1029/2007GC001805.

Gou Z, Zhang Z, Dong X, Xiang H, Ding H, Tian Z and Lei H (2016) Petrogenesis and tectonic implications of the Yadong leucogranites, southern Himalaya. *Lithos* 256–257, 300–10.

Groppo C, Rolfo F and Indares A (2013) Partial melting in the Higher Himalayan Crystallines of Eastern Nepal: the effect of decompression and implications for the 'Channel Flow' model. *Journal of Petrology* 53, 1057–88. doi: 10.1093/petrology/egs009.

Guillot S and Le Fort P (1995) Geochemical constraints on the bimodal nature of the High Himalayan leucogranites. *Lithos* 35, 221–34.

Guo Z and Wilson M (2012) The Himalayan leucogranites: constraints on the nature of their crustal source origin and geodynamic setting. *Gondwana Research* 22, 360–76. doi: 10.1016/j.gr.2011.07.027.

Harris N and Massey J (1994) Decompression and anatexis of Himalayan metapelites. *Tectonics* 13, 1537–46.

Harrison TM, Grove M, McKeegan KD, Coath CD, Lovera OM and Le Fort P (1999) Origin and episodic emplacement of the Manaslu intrusive complex, central Himalaya. *Journal of Petrology* 40, 3–19.

Harrison TM, Lovera OM and Grove M (1997) New insights into the origin of two contrasting Himalayan granite belts. *Geology* 25, 899–902.

Heim A and Gansser A (1939) Central Himalayas: geological observations of the Swiss Expedition in 1936. *Mémoires de la Société Helvétique des Sciences Naturelles* 73, 1–245.

Hopkinson TN, Harris NW, Warren CJ, Spencer CJ, Roberts NMW, Horstwood MSA and Parrish RR (2017) The identification and significance of pure sediment-derived granites. *Earth and Planetary Science Letters* 467, 57–63. doi: 10.1016/j.epsl.2017.03.018.

Horstwood MSA, Kosler J, Gehrels G, Jackson SE, McLean NM, Paton C, Pearson NJ, Sircombe K, Sylvester P, Vermeesch P, Bowring JF, Condon DJ and Schoene B (2016) Community-derived standards for LA-ICPMS U-(Th)-Pb geochronology: uncertainty propagation, age interpretation and data reporting. *Geostandards and Geoanalytical Research* 40, 311–32.

Horton F, Lee J, Hacker B, Bowman-Kamaha'o M and Cosca M (2015) Himalayan gneiss dome formation in the middle crust and exhumation by normal faulting: new geochronology of Gianbul dome, northwestern India. *Geological Society of America Bulletin* 127, 162–80.

Inger S and Harris N (1993) Geochemical constraints on leucogranite magmatism in the Langtang Valley, Nepal Himalaya. *Journal of Petrology* 34, 345–68.

King J, Harris N, Argles T, Parrish R and Zhang H (2011) Contribution of crustal anatexis to the tectonic evolution of Indian crust beneath Tibet. *Geological Society of America Bulletin* 123, 218–39. doi: 10.1130/B30085.1.

Le Fort P (1975) Himalaya: the collided range. Present knowledge of the continental arc. *American Journal of Science* 275A, 1–44.

Le Fort P (1986) Metamorphism and magmatism during the Himalayan collision. In *Collision Tectonics* (eds MP Coward and AC Ries), pp. 159–72. Geological Society of London, Special Publication no. 19.

Le Fort P, Cuney M, Deniel C, France-Lanord C, Sheppard SMF, Upreti BN and Vidal P (1987) Crustal generation of the Himalayan leucogranites. *Tectonophysics* 134, 39–57. doi: 10.1016/0040-1951(87)90248-4.

Lee J, Hacker BR, Dinklage WS, Wang Y, Gans P, Calvert A, Wan J-L, Chen W, Blythe AE and McClelland W (2000) Evolution of the Kangmar Dome, southern Tibet: structural, petrologic, and thermochronologic constraints. *Tectonics* 19, 872–96.

Lee J, Hacker BR and Wang Y (2004) Evolution of North Himalayan Gneiss Domes: structural and metamorphic studies in Mabja Dome, southern Tibet. *Journal of Structural Geology* 26, 2297–316.

Lee J, McClelland W, Wang Y, Blythe A and McWilliams M (2006) Oligocene-Miocene middle crustal flow in southern Tibet: geochronology of Mabja Dome. In *Channel Flow, Ductile Extrusion and Exhumation in Continental Collision* Zones (ed. RD Law), pp. 445–69. Geological Society, of London, Special Publication no. 268.

Lucas-Tooth HJ and Pyne C (1964) The accurate determination of major constituents by X-ray fluorescence analysis in the presence of large inter-element effects. *Advances in X-Ray Analysis* 7, 523–41.

Manickavasagam RM, Jain AK, Singh S, Asokan A, Macfarlane A, Sorkhabi R and Quade J (1999) Metamorphic evolution of the northwest Himalaya, India: pressure, temperature data, inverted metamorphism, and exhumation in the Kashmir, Himachal, and Garhwal Himalayas. *Geological Society of America Special* Paper 328, 179–98.

Meert JG and van der Voo R (1997) The assembly of Gondwana 800–550 Ma. *Journal of Geodynamics* 23, 223–35.

Metcalfe RP (1993) Pressure, temperature and time constraints on metamorphism across the Main Central Thrust zone and High Himalayan Slab in the Garhwal Himalaya. In *Himalayan Tectonics* (eds PJ Treloar and MP Searle), pp. 485–509. Geological Society of London, Special Publication no.74.

Miller C, Thöni M, Frank W, Grasemann B, Klötzli U, Guntli P and Draganits E (2001) The early Paleozoic magmatic event in the Northwest Himalaya, India: source, tectonic setting and age of emplacement. *Geological Magazine* 138, 237–51.

Montemagni C, Carosi R, Fusi N, Iaccarino S, Montomol, C, Villa IM and Zanchetta S (2020) Three-dimensional vorticity and time constrained evolution of the Main Central Thrust zone, Garhwal Himalaya (NW India). *Terra Nova* 32, 215–24.

Patiño Douce AE (1997) Generation of peraluminous A-type granites by low-pressure melting of calc-alkine granitoids. *Geology* 25, 743–66.

Patiño Douce AE and Harris N (1998) Experimental constraints on Himalayan anatexis. *Journal of Petrology* 39, 689–710.

Patiño Douce AE and McCarthy TC (1998) Melting of crustal rocks during continental collision and subduction. In *When Continents Collide: Geodynamics and Geochemistry of Ultrahigh-Pressure Rocks: Petrology and Structural Geology, v. 10* (eds BR Hacker and JG Liou), 27–55. Dordrecht: Springer. doi: 10.1007/978-94-015-9050-1_2.

Paton C, Hellstrom J, Paul B, Woodhead B and Hergt J (2011) Iolite: freeware for the visualisation and processing of mass spectrometric data. *Journal of Analytical Atomic Spectrometry* 26, 2508–18.

Pearce JA, Harris NB and Tindle AG (1984). Trace element discrimination diagrams for the tectonic interpretation of granitic rocks. *Journal of petrology*, 25(4), 956–983.

Pêcher A (1991) The contact between the Higher Himalayan Crystallines and the Tibetan sedimentary series: Miocene large-scale dextral shearing. *Tectonics* 10, 587–98.

Pêcher A and Scaillet B (1989) La structure du Haut-Himalaya au Garhwal (Indes). *Eclogae Geologicae Helevetiae* 82, 655–68.

Phukon P, Sen K, Singh PC, Sen A, Srivastava HB and Singhal S (2019) Characterizing anatexis in the Greater Himalayan Sequence (Kumaun, NW India) in terms of pressure, temperature, time and deformation. *Lithos* 344, 22–50. doi: 10.1016/j.lithos.2019.04.018.

Quigley M, Liangjun Y, Xiaohan L, Wilson CJL, Sandiford M and Phillips D (2006) [40]Ar/[39]Ar thermo-chronology of the Kampa dome, southern Tibet: implications for tectonic evolution of the North Himalayan gneiss domes. *Tectonophysics* 421, 268–97. doi: 10.1016/j.tecto.2006.05.002.

Rosenberg CL, Berger A and Schmid SM (1995) Observations from the floor of a granitoid pluton: inferences on the driving force of final emplacement. *Geology* 23, 443–6.

Scaillet B, Dardel J and Le Fort P (1988) A PêcherLes leucogranites de Gangotri (Himalaya du Garhwal), Résultats préliminairesRéu. Sci. Terre, 12th, p. 120(Lille).

Scaillet B, France-Lanord C and Le Fort P (1990) Badrinath-Gangotri plutons (Garhwal, India): petrological and geochemical evidence for fractionation processes in a High Himalayan Leucogranite. *Journal of Volcanology and Geothermal Research* 44, 163–88.

Scaillet B, Holtz F, Pichavant M and Schmidt M (1996) Viscosity of Himalayan leucogranites: implications for mechanisms of granitic magma ascent. *Journal of Geophysical Research* 101, 27,691–9.

Scaillet B, Pêcher A, Rochette P and Champenois M (1995) The Gangotri granite (Garhwal Himalaya): laccolithic emplacement in an extending collisional belt. *Journal of Geophysical Research: Solid Earth* 100, 585–607.

Searle MP (1999) Emplacement of Himalayan leucogranites by magma injection along giant sill complexes: examples from the Cho Oyu, Gyachung Kang and Everest leucogranites (Nepal Himalaya). *Journal of Asian Earth Sciences* 17, 773–83.

Sen K, Chaudhury R and Pfänder J (2015) [40]Ar-[39]Ar age constraint on deformation and brittle-ductile transition of the Main Central Thrust and South Tibetan Detachment Zone from Dhauliganga valley, Garhwal Himalaya. *Journal of Geodynamics* 88. doi: 10.1016/j.jog.2015.04.004.

Shand SJ (1943) *The Eruptive Rocks*, 2nd ed. New York: Wiley.

Singh S (2003) Himalayan Granitoids. *Journal of the Virtual Explorer* 11, 1–20.

Singh S (2018) Protracted zircon growth in migmatites and in-situ melt of Higher Himalayan Crystalline: U-Pb ages from Bhagirathi Valley, NW Himalaya, India. *Geoscience Frontiers*. doi: 10.1016/j.gsf.2017.12.014.

Singh S, Mukherjee PK, Jain AK, Khanna PP, Sain, NK and Kumar R (2003) Source characterization and possible emplacement mechanism of collision-related Gangotri Leucogranite along Bhagirathi Valley, NW-Himalaya. *Journal of the Virtual Explorer* 11, 15–26.

Sláma J, Kosler J, Condon DJ, Crowley JL, Gerdes A, Hanchar JM, Horstwood MSA, Morris GA, Nasdala L, Norberg N, Schaltegger U, Schoene B, Tubrett MN and Whitehouse MJ (2008) Plešovice zircon: a new natural reference material for U-Pb and Hf isotopic analysis. *Chemical Geology* 249, 1–35.

Sorkhabi RB, Stump E, Foland KA and Jain AK (1999) Tectonic and cooling history of the Garhwal High Himalaya (Bhagirathi Valley): constraining from thermochronological data. In *Geodynamics of the NW Himalaya* (eds. AK Jain and RM Manickavasgam), pp. 217–35. Gondwana Research Group Memoirs 6.

Spencer CJ, Kirkland CL and Taylor RJM (2016) Strategies towards statistically robust interpretations of in-situ U-Pb zircon geochronology. *Geoscience Frontiers* 7, 581–9.

Stern CR, Kligfield R, Schelling D, Fruta K and Virdi NS (1989) The Bhagirathi leucogranite of the High Himalaya: age, petrogenesis, and tectonic implications. *Geological Society of America Special Paper* 232, 33–45.

Taylor SR and McLennan SM (1985) *The Continental Crust, Its Composition and Evolution: An Examination of the Geochemical Record Preserved in Sedimentary Rocks.* Oxford: Blackwell, 312 pp.

Tripathi K, Sen K and Dubey AK (2012) Modification of fabric in pre-Himalayan granitic rocks by post-emplacement ductile deformation: insights from microstructures, AMS and U-Pb geochronology of the Paleozoic Kinnaur Kailash Granite and associated Cenozoic leucogranites of the South Tibetan Detachment Zone, Himachal High Himalaya. *International Journal of Earth Science* 101, 761–72.

Valdiya KS (1995) Proterozoic sedimentation and Pan-African geodynamic development in the Himalaya, the northern frontier of east Gondwanaland. *Gondwana Research* 1, 3–9.

Vermeesch P (2018) IsoplotR: a free and open toolbox for geochronology. *Geoscience Frontiers* 9, 1479–93.

Vigneresse JL, Tikoff B and Améglio L (1999) Modification of the regional stress field by magma intrusion and formation of tabular granitic plutons. *Tectonophysics* 302, 203–24.

Villaseca, C, Martín Romera C, De la Rosa J and Barbero L (2003) Residence and redistribution of REE, Y, Zr, Th and U during granulite-facies metamorphism: behaviour of accessory and major phases in peraluminous granulites of central Spain. *Chemical Geology* 200, 293–323. doi: 10.1016/s0009-2541(03)00200-6.

Visonà D, Carosi R, Montomoli C, Tiepolo M and Peruzzo L (2012) Miocene andalusite leucogranite in central-east Himalaya (Everest–Masang Kang area): low-pressure melting during heating. *Lithos* 144, 194–208. doi: 10.1016/j.lithos.2012.04.012.

Visonà D and Lombardo B (2002) Two-mica and tourmaline leucogranites from the Everest- Makalu region (Nepal-Tibet): Himalayan leucogranite genesis by isobaric heating? *Lithos* 62, 125–50.

Visonà D, Rubatto D and Villa IM (2010) The mafic rocks of Shao La (Kharta, S. Tibet): Ordovician basaltic magmatism in the greater Himalayan crystallines of central eastern Himalaya. *Journal of Asian Earth Sciences* 38, 14–25.

Wang X, Zhang J, Santosh M, Liu J, Yan S and Guo L (2012) Andean-type orogeny in the Himalayas of south Tibet: implications for early Paleozoic tectonics along the Indian margin of Gondwana. *Lithos* 154, 248–62. doi: 10.1016/j.lithos.2012.07.011.

Weinberg R, (2016) Himalayan leucogranites and migmatites: nature, timing and duration of anatexis. *Journal of Metamorphic Geology* 34, 821–43.

Wiedenbeck M, Alle P, Corfu F, Griffin WL, Meier M, Oberli F, von Quadt A, Roddick JC and Spiegel W (1995) Three natural zircon standards for U-Th-Pb, Lu-Hf, trace element and REE analyses. *Geostandard Newsletters* 19, 1–23.

Xu ZQ, Yang JS, Qi XX, Cui JW, Li HB and Chen FY (2006) India–Asia collision: a further discussion of N–S- and E–W-trending detachments and the orogenic mechanism of the modern Himalayas. *Geological Bulletin of China* 25, 1–14 (in Chinese with English abstract).

Yakymchuk C and Brown M (2019) Divergent behaviour of Th and U during anatexis: implications for the thermal evolution of orogenic crust. *Journal of Metamorphic Geology* **37**, 899–916. doi: 10.1111/jmg.12469.

Yakymchuk C, Kirkland CL and Clark C (2018) Th/U ratios in metamorphic zircon. *Journal of Metamorphic Geology* **36**, 715–37. doi: 10.1111/jmg.12307.

Yin A (2006) Cenozoic tectonic evolution of the Himalayan orogeny as constrained by along-strike variation of structural geometry, exhumation history and foreland sedimentation. *Earth Science Reviews* **76**, 1–131.

Zhang HF, Harris N, Parrish R, Kelley S, Zhang L, Rogers N, Argles T and King J (2004) Causes and consequences of protracted melting of the mid-crust exposed in the North Himalayan antiform. *Earth and Planetary Science Letters* **228**, 195–212.

Zhang HF, Harris N, Parrish R, Zhang L, Zhao ZD and Li DW (2005) Geochemistry of North Himalayan leucogranites: regional comparison, petrogenesis and tectonic implications. *Earth Science Journal of China University of Geosciences* **30**, 275–88 (in Chinese with English abstract).

Zhu DC, Zhao ZD, Niu YL, Dilek Y and Mo XX (2011) Lhasa terrane in southern Tibet came from Australia. *Geology* **39**, 727–30. doi: 10.1130/G31895.1.

Zhu DC, Zhao ZD, Niu YL, Dilek Y, Wang Q, Ji WH, Dong GC, Sui QL, Liu YS, Yuan HL and Mo XX (2012) Cambrian bimodal volcanism in the Lhasa Terrane, southern Tibet: record of an early Paleozoic Andean-type magmatic arc in the Australian proto-Tethyan margin. *Chemical Geology* **328**, 290–308. doi: 10.1016/j.chemgeo.2011.12.024.